ARTICLE

Interphase microtubule disassembly is a signaling cue that drives cell rounding at mitotic entry

Kévin Leguay[1,2] , Barbara Decelle[1,2], Islam E. Elkholi[4,9] , Michel Bouvier[1,3,5] , Jean-François Côté[4,5,7,8,9] , and Sébastien Carréno[1,2,6]

At mitotic entry, reorganization of the actomyosin cortex prompts cells to round-up. Proteins of the ezrin, radixin, and moesin family (ERM) play essential roles in this process by linking actomyosin forces to the plasma membrane. Yet, the cell-cycle signal that activates ERMs at mitotic entry is unknown. By screening a compound library using newly developed biosensors, we discovered that drugs that disassemble microtubules promote ERM activation. We further demonstrated that disassembly of interphase microtubules at mitotic entry directs ERM activation and metaphase cell rounding through GEF-H1, a Rho-GEF inhibited by microtubule binding, RhoA, and its kinase effector SLK. We finally demonstrated that GEF-H1 and Ect2, another Rho-GEF previously identified to control actomyosin forces, act together to drive activation of ERMs and cell rounding in metaphase. In summary, we report microtubule disassembly as a cell-cycle signal that controls a signaling network ensuring that actomyosin forces are efficiently integrated at the plasma membrane to promote cell rounding at mitotic entry.

Introduction

Cell morphogenesis relies on a dynamic reorganization of the actomyosin cortex (Diz-Munoz et al., 2013). Forces generated by actomyosin contractions are coupled to the plasma membrane and apply tension that drives cell shape remodeling. During mitosis, coordination between cell morphogenesis and chromosome segregation preserves genome stability (Ramkumar and Baum, 2016). Deregulation of this coordination leads to aneuploidy that contributes to growth and developmental defects and to cancers (Ben-David and Amon, 2020).

Early in mitosis, the cortex stiffens up isotropically, a mechanism that participates in promoting mitotic rounding (Kunda et al., 2008). At least two other mechanisms were also identified to contribute to this mitotic rounding. Changes in cell osmolarity promote osmotic swelling in prophase and metaphase (Son et al., 2015; Stewart et al., 2011; Zlotek-Zlotkiewicz et al., 2015), and cell-substratum adhesion structures are disassembled while cells enter into mitosis (Dao et al., 2009; Marchesi et al., 2014; Yamakita et al., 1999). Almost every animal cell is spherical in metaphase. Rounding is necessary for the biogenesis of the spindle and for chromosome centering by limiting the space that microtubules have to search for chromosomes (Lancaster et al., 2013). Cortical stiffening also protects

the division apparatus from external forces that can be exerted by neighboring cells in tissues (Matthews et al., 2012; Matthews et al., 2020).

Two independent signaling pathways were shown to control reorganization of cortical actomyosin forces in metaphase cells (Taubenberger et al., 2020). On the one hand, the M-phase promoting factor, Cdk1/Cyclin B, phosphorylates Ect2, a Rho guanine nucleotide exchange factor (Rho-GEF) that activates RhoA. This small GTPase promotes the actomyosin contractions necessary for cell rounding by activating actin polymerization through formins and myosin light chain II phosphorylation through Rho-associated protein kinases (ROCK; Maddox and Burridge, 2003; Matthews et al., 2012). On the other hand, we and others have shown that in *Drosophila*, dMoesin, the sole ortholog of the ezrin–radixin–moesin (ERM) family of proteins, drives metaphase rounding by functionally linking the newly generated actomyosin forces to the plasma membrane. While the role of ERM proteins in mitotic rounding of mammalian cells still remains to be established, depletion of dMoesin promotes defects in cortical stiffness and metaphase cell rounding in *Drosophila* cells in culture (Carreno et al., 2008; Kunda et al., 2008).

....
[1]Institute for Research in Immunology and Cancer, Université de Montréal, Montréal, Quebec, Canada;   [2]Cellular Mechanisms of Morphogenesis during Mitosis and Cell Motility lab, Université de Montréal, Montréal, Quebec, Canada;   [3]Molecular Pharmacology Lab, Université de Montréal, Montréal, Quebec, Canada;   [4]Montréal Clinical Research Institute, Montréal, Quebec, Canada;   [5]Department of Biochemistry and Molecular Medicine, Université de Montréal, Montréal, Quebec, Canada;   [6]Department of Pathology and Cell Biology, Université de Montréal, Montréal, Quebec, Canada;   [7]Department of Medicine, McGill University, Montréal, Quebec, Canada;   [8]Department of Anatomy and Cell Biology, McGill University, Montréal, Quebec, Canada;   [9]Cytoskeletal Organization and Cell Migration lab, Université de Montréal, Montréal, Quebec, Canada.

Correspondence to Sébastien Carréno: sebastien.carreno@umontreal.ca.

ERM crosslink actin filaments (F-actin) and microtubules with the plasma membrane (Fehon et al., 2010; Solinet et al., 2013). ERMs exist at the plasma membrane under a closed-inactive and open-active conformations (Leguay et al., 2021). When closed, their N-terminal four-point-one, ezrin, radixin, moesin (FERM) domain binds their C-terminal actin-binding domain (C-ERMAD) and ERMs cannot link F-actin or microtubules to the plasma membrane (Gary and Bretscher, 1995; Solinet et al., 2013). Ser/Thr kinases open ERMs by phosphorylating a conserved Thr residue (T567, T564, and T558 in ezrin, radixin, and moesin, respectively) thereby freeing their C-ERMAD and FERM, which are then accessible to interact with F-actin and microtubules, respectively (Pelaseyed et al., 2017). In *Drosophila* and human cells, ERMs were shown to be phosphorylated and activated at mitotic entry by the Ser/Thr kinases of the Ste20-like kinase (SLK) family (Carreno et al., 2008; De Jamblinne et al., 2020; Kunda et al., 2008; Machicoane et al., 2014; Roubinet et al., 2011). However, the cell-cycle signal that prompts activation of ERMs when cells enter into mitosis is still unknown.

In this study, we found that disassembly of microtubules activates ERMs. We showed that GEF-H1 acts downstream of interphase microtubule disassembly at mitotic entry to promote cell rounding by activating ERMs via RhoA and its kinase effector SLK. In addition, we demonstrated that GEF-H1 and Ect2 act together to drive ERM activation and cell rounding in metaphase. We thus identified interphase microtubule disassembly as a cell-cycle signal that contributes to a signaling network ensuring that actomyosin forces are efficiently coupled to the plasma membrane to promote proper cell rounding in metaphase.

Results

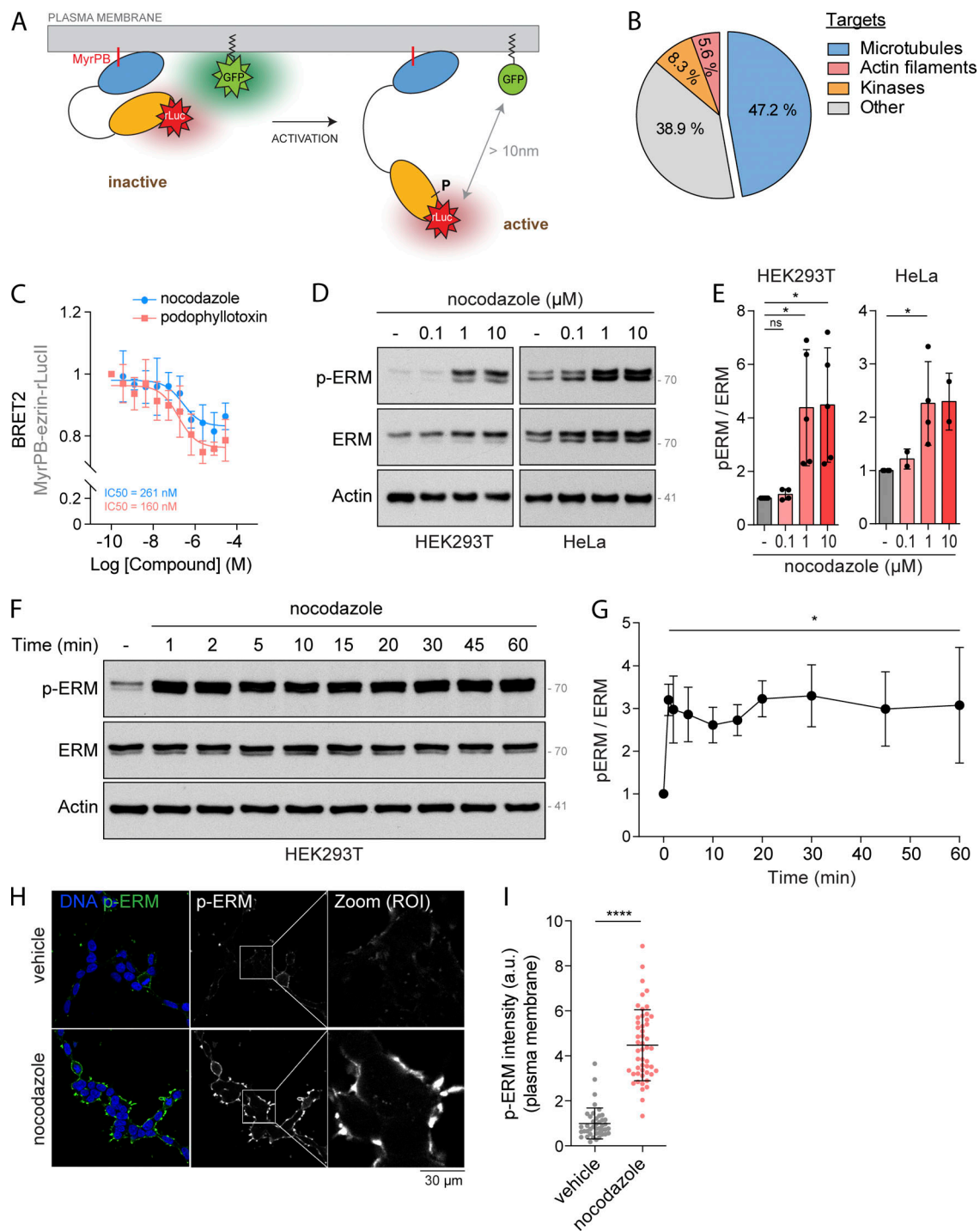### Drugs that disassemble microtubules promote ERM activation

To study the regulation of ERMs in live cells, we recently designed ERM bioluminescence resonance energy transfer (BRET)–based biosensors (Leguay et al., 2021). Briefly, the bioluminescent donor (*Renilla* luciferase, rLucII) is fused to the C-terminus of individual ERMs that are anchored at the plasma membrane through a myristoylation and polybasic (MyrPB) motif (MyrPB-E,R,M-rLucII; Fig. 1 A). The rGFP (*Renilla* GFP) acceptor is also targeted to the plasma membrane through the prenylation CAAX box of Kirsten rat sarcoma viral oncogene homolog (KRAS; rGFP-CAAX, Fig. 1 A). Since BRET occurs only when the acceptor and donor are in close proximity (<10 nm; Breton et al., 2010), ERM opening and activation decrease BRET2 signals, whereas ERM closing and inactivation increase these signals.

Using the MyrPB-ezrin-rLucII BRET biosensor, we screened a library of 3,469 FDA-approved small molecules in human embryonic kidney cells (HEK293T). Among the 46 candidates promoting BRET2 signal decrease (Fig. S1, A and B), we identified 36 molecules that activate ezrin in a confirmation screen (Fig. S1 C). Although a link between ERM activation and microtubules has never been established to our knowledge, we found that molecules that promote microtubule disassembly were over-

represented among these activators (17 out of 36 molecules; Figs. 1 B and S1 C). By performing dose-response experiments with two of these microtubule destabilizing drugs, we found that nocodazole and podophyllotoxin promote ezrin opening at IC50 compatible with their action on microtubule disassembly (261 nM and 160 nM, respectively; Figs. 1 C and S1 D). Next, we confirmed that microtubule disassembly activates ERMs by assessing the phosphorylation of their common regulatory Thr using a well-characterized anti–p-ERM antibody (Carreno et al., 2008). We found that microtubule disassembly promotes ERM phosphorylation in HEK293T cells, as well as in the five other human and murine cell lines tested (Fig. 1, D and E; and Fig. S1, E and G). We also found that in HEK293T cells, ERMs are activated after 1 min of nocodazole treatment, the earliest time point tested (Fig. 1, F and G). Finally, we found that ERMs are phosphorylated at the plasma membrane upon nocodazole-induced microtubule disassembly (Fig. 1, H and I; and Fig. S1, H and I).

GEF-H1 and RhoA act downstream of nocodazole-induced microtubule disassembly to activate ERMs

We next aimed to determine how microtubule disassembly promotes ERM activation. We previously reported that ERMs directly bind to microtubules through a conserved charged motif within their FERM domain (Solinet et al., 2013). However, we found that ERM activation by nocodazole is not dependent on their direct interaction with microtubules since an ezrin microtubule-binding mutant (ezrin^{KK211,212MM}) was still phosphorylated after nocodazole treatment (Fig. S1 J). Nocodazole-induced microtubule disassembly may thus activate ERMs through other downstream signaling molecules. Interestingly, nocodazole has been shown to trigger RhoA activation through the release of GEF-H1, a Rho-GEF, from microtubules (Chang et al., 2008; Krendel et al., 2002). Furthermore, other studies have established that RhoA could mediate activation of ERMs (Kotani et al., 1997; Shaw et al., 1998). We then tested if RhoA and GEF-H1 could mediate the signal from nocodazole-induced microtubule disassembly to ERM activation. As previously observed in HeLa and D2 cells (Chang et al., 2008; Krendel et al., 2002), we confirmed that nocodazole treatment activates RhoA in HEK293T cells using a rhotekin-RBD (Rho binding domain) pulldown assay that reveals the fraction of active RhoA bound to GTP (Fig. 2, A and B). We then used the exoenzyme C3 transferase to inhibit RhoA and test the function of this small GTPase in ERM activation. Demonstrating that the exoenzyme C3 transferase properly inhibited RhoA in HEK293T cells, and as previously established (Majumdar et al., 1998), we observed that it substantially decreased the phosphorylation of myosin light chain II in control cells (Fig. S2, A and B). In addition, we found that chemical inhibition of RhoA also abrogates ERM activation after nocodazole-induced microtubule disassembly (Fig. 2, C and D). We next established that activation of ERMs upon microtubule disassembly is also mediated by GEF-H1, which is inhibited by its binding to microtubules (Birukova et al., 2006; Chang et al., 2006; Krendel et al., 2002; Matsuzawa et al., 2004; Ren et al., 1998). Depletion of GEF-H1 using independent shRNA or siRNA decreased ERM phosphorylation after nocodazole treatment (Fig. 2, E and F; and Fig. S2, C and D). We also noticed that

Leguay et al.
Signals that prompt metaphase cell rounding

Journal of Cell Biology 2 of 17
https://doi.org/10.1083/jcb.202109065

Figure 1. **Drugs that disassemble microtubules promote ERM activation. (A)** Schematic representation of MyrPB-ezrin-rLucII/rGFP-CAAX BRET2 biosensor (Leguay et al., 2021). **(B)** Diagram representing the identified class of targets of the validated ezrin activators. **(C)** BRET2 signals were measured in HEK293T cells expressing MyrPB-ezrin-rLucII/rGFP-CAAX and incubated with increasing concentration of nocodazole (blue) or podophyllotoxin (red) for 15 min. **(D and E)** Immunoblot of HEK293T (left) and HeLa (right) cells incubated with the indicated concentrations of nocodazole for 15 min (D). p-ERM over ERM signals were quantified and normalized to vehicle (DMSO; E). **(F and G)** Immunoblot of HEK293T cells incubated with 1 µM nocodazole for the indicated times (F). p-ERM over ERM signals were quantified and normalized to vehicle (t = 0; G). **(H and I)** Immunofluorescence of HEK293T cells incubated with vehicle (DMSO) or 1 µM nocodazole for 15 min (H). p-ERM staining at the plasma membrane was quantified and normalized to cells treated with vehicle (I; n > 45 cells). BRET2 signals (C) represent the mean ± SD of three independent experiments. Immunoblots (D and F) and immunofluorescences (H) are representative of at least two independent experiments. p-ERM quantifications represent the mean ± SD of at least two independent experiments. Dots represent independent experiments (E), individual cells (I), or the mean of independent experiments (C and G). P values were calculated using one-sample t test (E and G) or using two-tailed unpaired t test (I). *, P < 0.05; ****, P < 0.0001. ns, not significant. Numbers associated with Western blots indicate molecular weight in kD. Source data are available for this figure: SourceData F1.
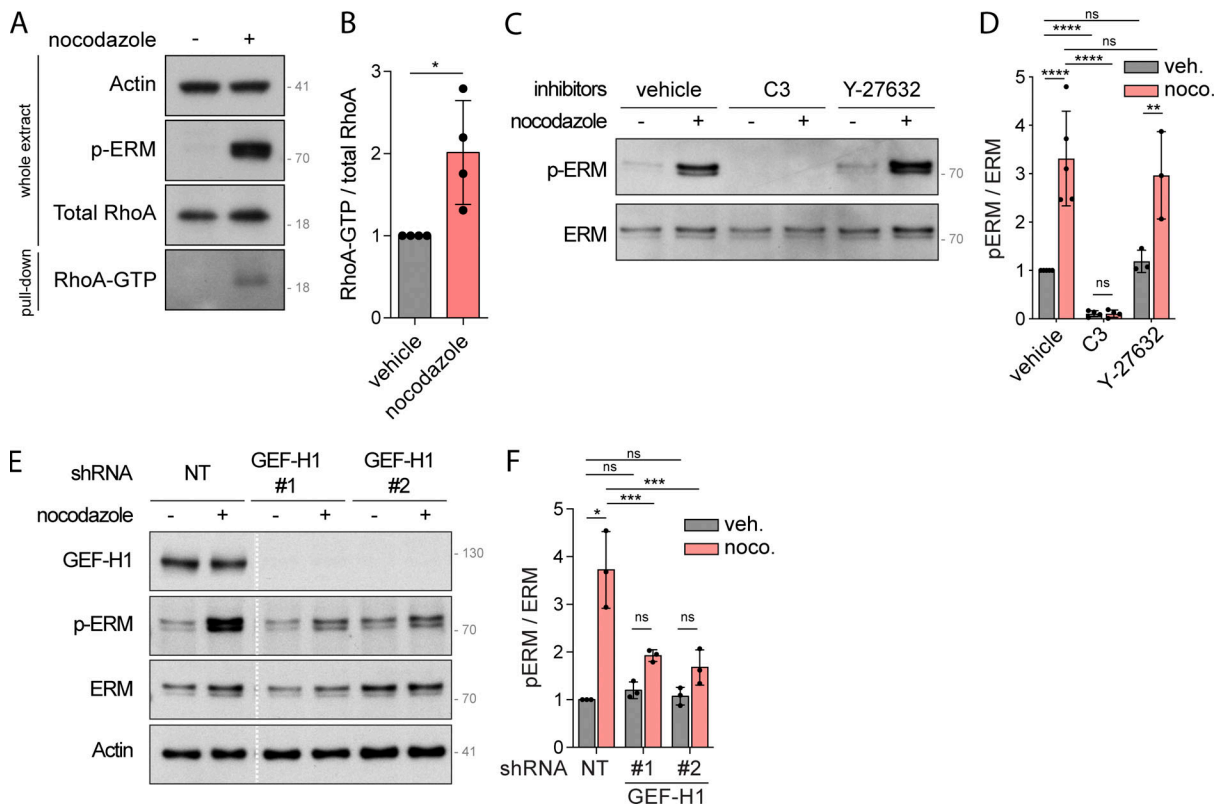
Figure 2. **GEF-H1 and RhoA activate ERMs downstream of nocodazole-induced microtubule disassembly. (A and B)** Rhotekin-RBD pull-down assays were performed to evaluate RhoA activation. Immunoblot of whole extract HEK293T cells incubated with vehicle (DMSO) or 1 µM nocodazole for 15 min are shown in the three top panels. Pull-down RhoA is shown in the lower panel (A). RhoA-GTP over total RhoA were quantified and normalized to vehicle (B). **(C and D)** Immunoblot of HEK293T cells pre-incubated with vehicle (DMSO), 1 µg/ml C3 transferase for 6 h or 10 µM Y-27632 for 4 h and then incubated with vehicle (DMSO) or 1 µM nocodazole for 15 min (C). p-ERM over ERM signals were quantified and normalized to vehicle (D). **(E and F)** Immunoblot of HEK293T cells stably expressing non-target shRNA (NT) or two different shRNA targeting GEF-H1 and incubated with vehicle (DMSO) or 1 µM nocodazole for 15 min. White lines indicate that intervening lanes have been spliced out (E). p-ERM over ERM signals were quantified and normalized to NT treated with vehicle (F). Immunoblots (A, C, and E) are representative of at least three independent experiments. p-ERM quantifications represent the mean ± SD of at least three independent experiments. Dots represent independent experiments (B, D, and F). P values were calculated using one-sample *t* test (B) or using Holm-Sidak's multiple comparisons test with a single pooled variance (D and F) except for comparison made with normalized condition (vehicle + vehicle [D] or NT + vehicle [F]) where one-sample *t* test was applied. *, P < 0.05; **, P < 0.01; ***, P < 0.001; ****, P < 0.0001. Numbers associated with Western blots indicate molecular weight in kD. Source data are available for this figure: SourceData F2.

GEF-H1 depletion does not affect ERM phosphorylation in cells with intact microtubules, unlike inhibition of RhoA (Fig. 2, C–F; and Fig. S2, C and D). This indicates that GEF-H1 activates ERMs only downstream of microtubule disassembly whereas RhoA controls the overall level of ERM activation.
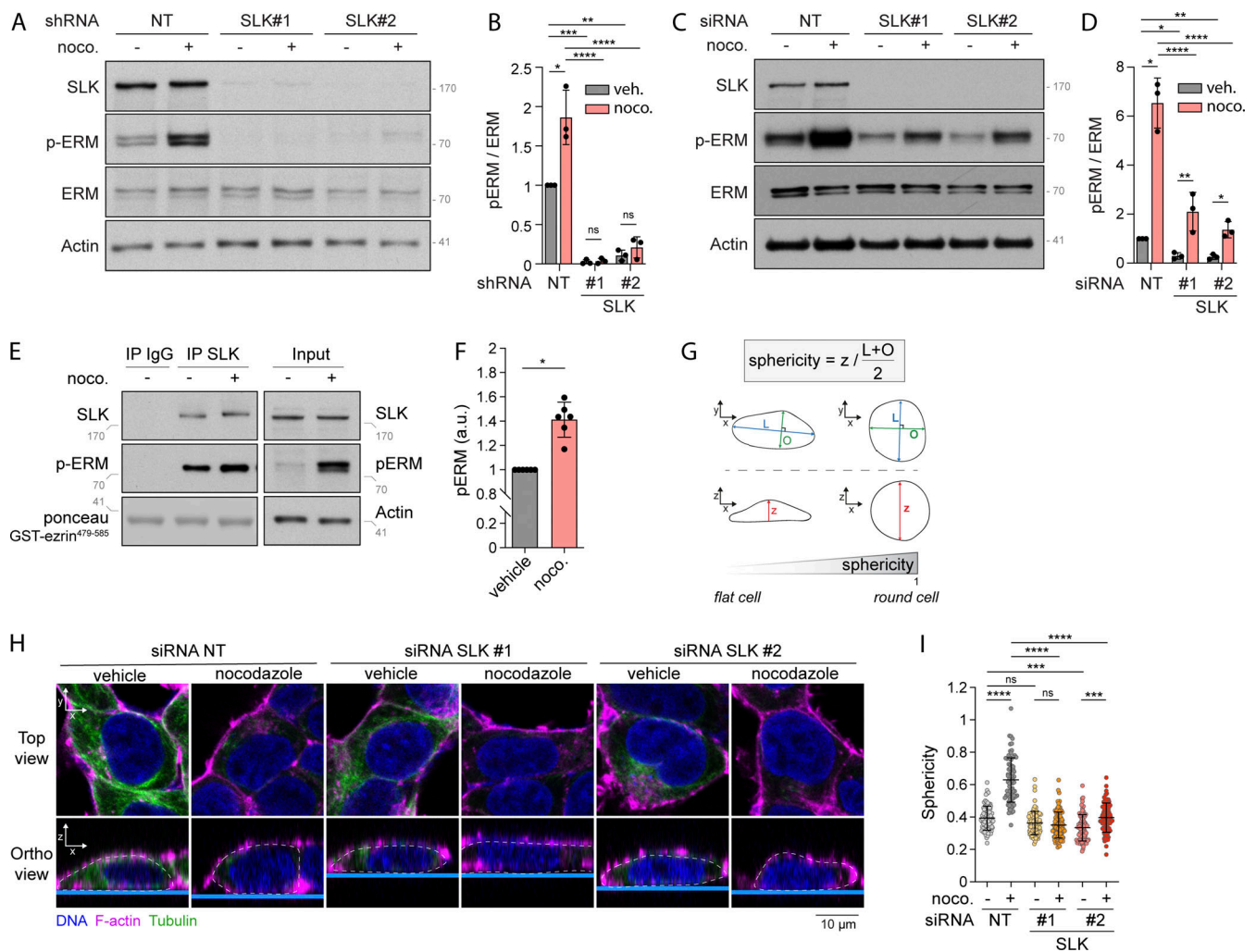
Nocodazole-induced microtubule disassembly promotes interphase cell rounding through SLK activation

We then aimed to identify which kinase acts downstream of GEF-H1 and RhoA to phosphorylate ERMs upon nocodazole treatment. Two different Ser/Thr kinases, SLK and ROCK, have been identified to be directly activated by RhoA (Bagci et al., 2020; Fujisawa et al., 1998; Sahai et al., 1999) and to directly phosphorylate ERMs (Machicoane et al., 2014; Matsui et al., 1999; Viswanatha et al., 2012). We then investigated if these kinases could phosphorylate ERMs downstream of nocodazole-induced microtubule disassembly. We found that inhibition of ROCK1 and ROCK2 using Y-27632 did not decrease ERM phosphorylation after nocodazole treatment (Fig. 2, C and D). Yet, Y-

27632 properly inhibited ROCK kinase activities since phosphorylation of myosin light chain II, a well-characterized ROCK substrate (Totsukawa et al., 2000), is almost suppressed (Fig. S2, A and B).

On the contrary, we found that SLK stable depletion using independent shRNA abrogates ERM phosphorylation both in nontreated cells and upon nocodazole treatment (Fig. 3, A and B). While this shows that SLK phosphorylates ERMs downstream of microtubule disassembly, we observed that SLK stable depletion promotes defects in cell growth and adhesion (data not shown). We thus further investigated the importance of SLK for ERM phosphorylation by transiently depleting this kinase using independent siRNA. After 48 h of SLK siRNA transfection, we confirmed that this kinase is necessary for microtubule-dependent ERM activation (Fig. 3, C and D). In accordance with these results, we found that microtubule disassembly activates the kinase activity of SLK using an in vitro kinase assay with immunoprecipitated SLK from cells treated with nocodazole (Fig. 3, E and F). We also found that this was not a direct

Figure 3. **Nocodazole-induced microtubule disassembly promotes interphase cell rounding depending on SLK activation. (A–D)** Immunoblots of HEK293T cells stably expressing non-target shRNA (NT) or two independent shRNA targeting SLK (A) or HEK293T cells transiently transfected with non-target siRNA (NT) or two independent siRNA targeting SLK (C) and incubated with vehicle (DMSO) or 1 μM nocodazole (noco.) for 15 min. p-ERM over ERM (B) or actin (D) signals were quantified and normalized to NT incubated with vehicle (B and D). **(E and F)** Kinase assay of endogenous SLK immunoprecipitated from HEK293T cells incubated with vehicle (DMSO) or 1 μM nocodazole for 15 min. Total lysate (input) is shown in the right panels (E). p-ERM signals were quantified and normalized to vehicle (F). **(G–I)** Measurement of cell sphericity in HEK293T cells incubated with the indicated treatments. **(I)** Cell sphericity was quantified as a ratio between cell height (z) and cell shape within the x/y plane, which is determined as the average length of the longer axis (L) and its orthogonal (O); see G and Material and methods section for more details. **(H)** F-actin, red; tubulin, green; DNA, blue. Dashed white lanes underline cell periphery in the orthogonal view. Top panels show confocal planes (Top view), and lower panels show orthogonal views (Ortho view; n > 80 cells). p-ERM and sphericity quantifications represent the mean ± SD of at least three independent experiments. Dots represent independent experiments (B, D, and F) or individual cells (I). P values were calculated using one-sample t test (F) or using Holm-Sidak's multiple comparisons test with a single pooled variance (B, D, and I) except for comparison made with normalizing condition (NT + vehicle [B and D]) where one-sample t test was applied. *, P < 0.05; **, P < 0.01; ***, P < 0.001; ****, P < 0.0001. Numbers associated with Western blots indicate molecular weight in kD. Source data are available for this figure: SourceData F3.

effect of nocodazole on the enzyme since this molecule did not affect the kinase activity of a recombinant SLK in vitro (Fig. S2 E).

Nocodazole treatment was previously found to promote cell rounding in interphase dependently on GEF-H1 (Chang et al., 2008). We extended these findings by showing that the effect of nocodazole on cell rounding is dependent on SLK using 3D reconstruction after confocal microscopy. Indeed, upon microtubule disassembly, transient depletion of SLK prevented the increase of cell sphericity, calculated as the ratio between cell height and cell shape in the x/y plane (see Material and methods

section for more details; Fig. 3, G–I). Altogether, these experiments indicate that nocodazole-induced microtubule disassembly promotes cell rounding in interphase by activating SLK.

Perturbing interphase microtubule disassembly at mitotic entry inhibits ERM activation

At mitotic entry, CDK1 was shown to promote interphase microtubule array disassembly by inactivating microtubule-associated protein 7 (MAP7), a microtubule-stabilizing protein (McHedlishvili et al., 2018). We therefore hypothesized that disassembly of interphase microtubules acts as a signaling cue

that promotes ERM activation at mitotic entry. To test this hypothesis, we first treated cells with low doses of taxol (paclitaxel), a treatment that was previously demonstrated to perturb disassembly of the interphase microtubule array while cells enter into mitosis (Leung and Cassimeris, 2019; McHedlishvili et al., 2018). We treated cells with this microtubule stabilizing drug for 90 min to allow cells that reach metaphase to have previously gone through the interphase-to-mitosis transition during the taxol treatment. While ERM phosphorylation increased more than threefold from interphase to metaphase in control cells, we found that low doses of taxol partially inhibit ERM phosphorylation in metaphase but did not affect the levels of phosphorylated ERMs in interphase cells (Fig. 4, A and B). Disassembly of interphase microtubule was also proposed to free tubulin dimers that can then repolymerize to form the mitotic spindle (Zhai et al., 1996). In agreement with this latter function (Hornick et al., 2008), we found that low dose of taxol affects the formation of the mitotic spindle, with an increase of monopolar spindles in metaphase, as well as an increased number of mitotic cells (Fig. S2, F–H). Excluding an effect of taxol on ERM phosphorylation, independent of its action perturbing interphase microtubule disassembly at mitosis entry, we showed that treatment of cells with taxol for 15 min did not affect ERM phosphorylation in metaphase when compared with cells treated with vehicle (Fig. S2, I and J). Unlike the 90-min taxol treatment, this short 15-min treatment does not allow cells that enter mitosis to reach metaphase. Altogether, our results support that interphase microtubule disassembly acts as a signaling cue that drives ERM activation at mitosis entry.

A GEF-H1–RhoA–SLK signaling axis activates ERMs downstream of interphase microtubule disassembly at mitotic entry

We then tested if mitotic disassembly of interphase microtubules could engage the same signaling network that activates ERMs after nocodazole treatment. We first found that GEF-H1 depletion using independent siRNA or shRNA decreased ERM phosphorylation in metaphase (Fig. 4, C and D; and Fig. S2, K and L). We then showed that RhoA chemical inhibition or transient SLK depletion almost totally abrogate phosphorylation of ERMs in metaphase (Fig. 4, E–H). While both RhoA inhibition and SLK depletion also abrogate ERM phosphorylation in interphase, we observed that GEF-H1 depletion affects ERM phosphorylation in mitosis only (Fig. 4, D, F, and H). To our knowledge, GEF-H1 is the first protein that was identified to promote ERM activation, specifically in mitosis. Finally, if the GEF-H1–dependent pathway transmits signals from interphase microtubule disassembly to ERM activation in metaphase, we reasoned that the requirement of interphase microtubule disassembly could be bypassed by activating RhoA. We used CN03, a small molecule that was shown to activate RhoA to test this hypothesis (Schmidt et al., 1997). We first validated the efficacy of this RhoA activator by showing that CN03 promotes the phosphorylation of ERMs and myosin light chain II, two downstream indirect effectors of RhoA, in control cells (Fig. S2, A, B, M, and N). Confirming our hypothesis, we then found that this RhoA activator restores normal metaphase levels of p-ERMs in cells where interphase

microtubule disassembly was impaired by low levels of taxol (Fig. 4, I and J). Altogether, these results demonstrate that the disassembly of interphase microtubules acts as a cell-cycle cue that engages GEF-H1, RhoA, and SLK to promote ERM activation upon entering into mitosis.
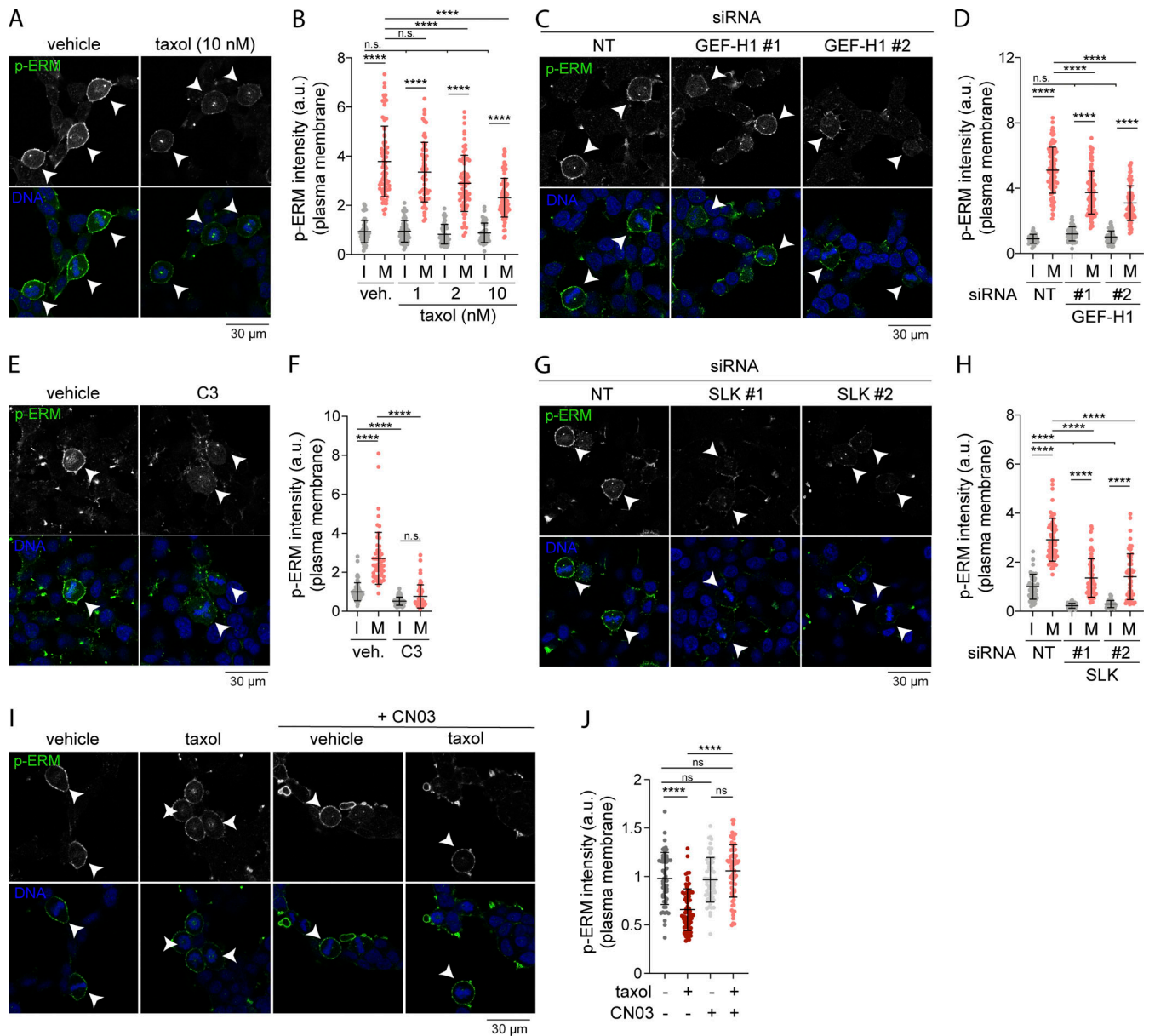
SLK and ERMs promote cell rounding in metaphase

Slik and dMoesin, the fly orthologs of SLK and ERMs, respectively, were shown to play crucial roles in cell rounding of *Drosophila* metaphase cells (Kunda et al., 2008). Yet, the involvement of SLK and ERMs and their respective mammalian orthologs for metaphase cell rounding remains to be established. We found that the transient knockdown of SLK led to a decrease in metaphase cell sphericity and cell height in comparison with control metaphase cells (Fig. 5, A and B; and Fig. S3 A). Accordingly, SLK-depleted metaphase cells appeared more spread out as measured by the increase of cell dimensions within the x/y plane (Fig. S3 B). To further quantify cell rounding from interphase to metaphase, we measured the ratio of sphericity between the two populations of interphase and metaphase cells. We found that SLK depletion significantly reduced this ratio (Fig. 5 C), demonstrating that, as previously established for its *Drosophila* ortholog, SLK plays an important role in metaphase cell rounding in mammalian cells. We also observed similar sphericity defects in metaphase cells upon co-depletion of the three ERM proteins (Fig. 5, D–G; and Fig. S3, C and D), suggesting that ERM phosphorylation by SLK is required for rounding at mitotic entry in mammalian cells. To further test this hypothesis, we wondered if the expression of a constitutively active phosphomimetic mutant of one of the ERM proteins would compensate for the loss of SLK. While a substantial decrease of metaphase cell sphericity was observed in SLK-depleted cells, this was completely rescued by expression of ezrin^{T567D} but not of ezrin^{T567A}, its non-phosphorylatable mutant (Fig. 5, H–J; and Fig. S3, E and F). We also observed that expression of ezrin^{T567A} in control cells decreases sphericity and cell height of metaphase cells (Fig. 5, I and J; and Fig. S3 E). This is in accordance with this construct behaving as a dominant negative ERM mutant (Gautreau et al., 2000) and further demonstrates the important role of ERMs for metaphase cell rounding.

Interphase microtubule disassembly at mitotic entry controls cell rounding

We next wondered if by activating the GEF-H1–RhoA–SLK–ERM signaling axis, the disassembly of interphase microtubule at mitotic entry could promote cell rounding in metaphase. We first showed that perturbing interphase microtubule disassembly prevents metaphase cell rounding. We measured decreases of metaphase cell sphericity and cell height, as well as ratio of sphericity between interphase and metaphase in cells treated with low dose of taxol for 90 min (Fig. 6, A–C; and Fig. S4, A and B). Importantly, as previously observed for ERM phosphorylation (Fig. S2, I and J), a short 15-min treatment with taxol did not affect cell sphericity or cell height in metaphase cells (Fig. S4, C–F).

We next showed that in agreement with its role on ERM activation in metaphase, GEF-H1 drives interphase to metaphase
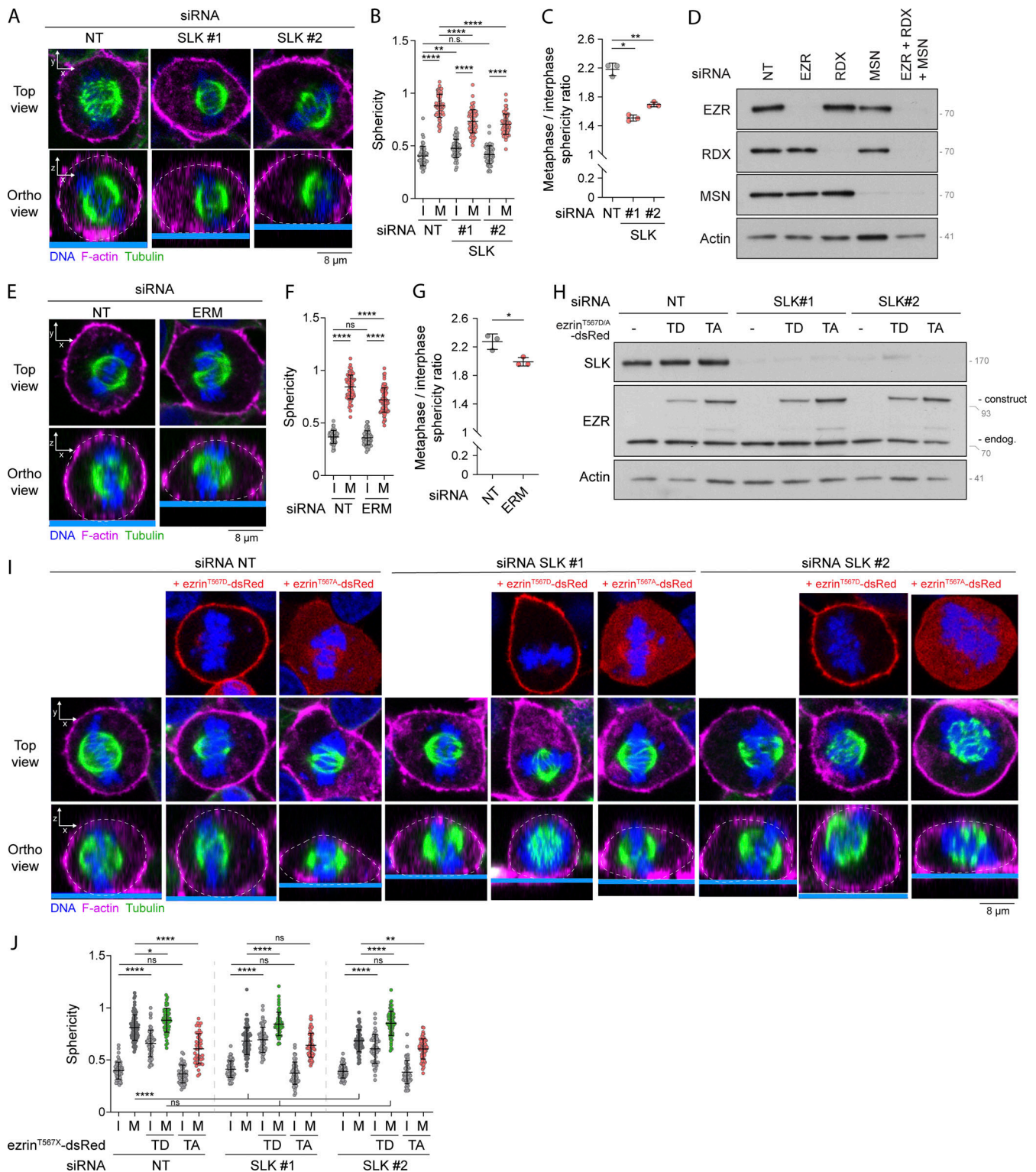
Leguay et al.
Signals that prompt metaphase cell rounding

Journal of Cell Biology   6 of 17
https://doi.org/10.1083/jcb.202109065

Figure 4. **Perturbing interphase microtubule disassembly at mitotic entry inhibits ERM activation in metaphase. (A–J)** Immunofluorescences of HEK293T cells incubated with vehicle (DMSO) or indicated concentrations of taxol for 90 min (A and B; n > 70 cells), transiently transfected with non-target siRNA (NT) or two independent siRNA targeting GEF-H1 (C and D; n > 80 cells) or two independent siRNA targeting SLK (G and H; n > 45 cells), incubated with vehicle (veh.; water) or 1 µg/ml C3 transferase (C3) for 6 h (E and F; n > 55 cells), incubated with vehicle (DMSO) or 10 nM taxol for 90 min and/or 1 µg/ml Rho activator II (CN03) for 1 h (I and J; n > 55 cells). Metaphase and interphase cells were identified based on DNA staining (DAPI, blue; A, C, E, G, and I; arrowheads indicate metaphase cells), and p-ERM (green) signal intensity at the plasma membrane was quantified and normalized to interphase cells incubated with vehicle (B and F), to interphase cells treated with non-target siRNA (D and H), or to metaphase cells incubated with vehicle (J). I, interphase; M, metaphase. Immunofluorescences (A, C, E, G, and I) are representative of three independent experiments. p-ERM quantifications represent the mean ± SD of three independent experiments, and dots represent individual cells. P values were calculated using Holm-Sidak's multiple comparisons test with a single pooled variance. ****, P < 0.0001.

cell rounding. Depletion of GEF-H1 using siRNA or shRNA decreased sphericity and cell height in metaphase, as well as ratio of sphericity between interphase and metaphase (Fig. 6, D–F; and Fig. S4, G–M). While GEF-H1 was previously shown to control cytokinesis (Birkenfeld et al., 2007), we present here the first evidence that this Rho-GEF plays also important roles in an earlier stage of mitosis. Then, and as already reported by others (Maddox and Burridge, 2003; Matthews et al., 2012;

Ramanathan et al., 2015), we showed that RhoA was necessary for metaphase cell rounding by inhibiting this GTPase using the exoenzyme C3 transferase (Fig. 6, G–I; and Fig. S4, N and O). Finally, having previously established that RhoA chemical activation bypasses the need for interphase microtubule disassembly to activate ERMs in metaphase (see Fig. 4, I and J), we showed that the RhoA activator CN03 also rescues mitotic rounding defects caused by treatment with low doses of taxol

Leguay et al.
Signals that prompt metaphase cell rounding

Journal of Cell Biology   7 of 17
https://doi.org/10.1083/jcb.202109065

Figure 5. **SLK and ERMs promote cell rounding in metaphase. (A–J)** Sphericity and mitotic rounding defects were measured using immunofluorescence 3D reconstitution after confocal microscopy in HEK293T cells transiently transfected with non-target siRNA (NT) or two independent siRNA targeting SLK (A–C; n > 55 cells) or a combination of three siRNA targeting each ERM (D–G; n > 55 cells), or transiently transfected with non-target siRNA (NT) or two independent siRNA targeting SLK and co-transfected with ezrin[T567D]-dsRed or ezrin[T567A]-dsRed constructs (H–J; n > 48 cells). **(A, E, and I)** Top panels show confocal planes (Top view), and lower panels show orthogonal views (Ortho view). Sphericity was measured as in Fig. 3 G (B, F, and J). Mitotic rounding defects were assessed by measuring the mean sphericity ratio of metaphase to interphase cell populations (C and G). Knock down efficiency and overexpression were assessed using immunoblots (D and H). Immunofluorescences (A, E, and I) and immunoblots (D and H) are representative of three independent experiments. Quantifications of sphericity and sphericity ratio of metaphase to interphase populations represent the mean ± SD of three independent experiments. Dots represent individual cells (B, F, and J) or independent experiments (C and G). P values were calculated using Holm-Sidak's multiple comparisons test with a single pooled variance (B, F, and J) or using a two-tailed paired t test (C and G). *, P < 0.05; **, P < 0.01; ****, P < 0.0001. Numbers associated with Western blots indicate molecular weight in kD. Source data are available for this figure: SourceData F5.
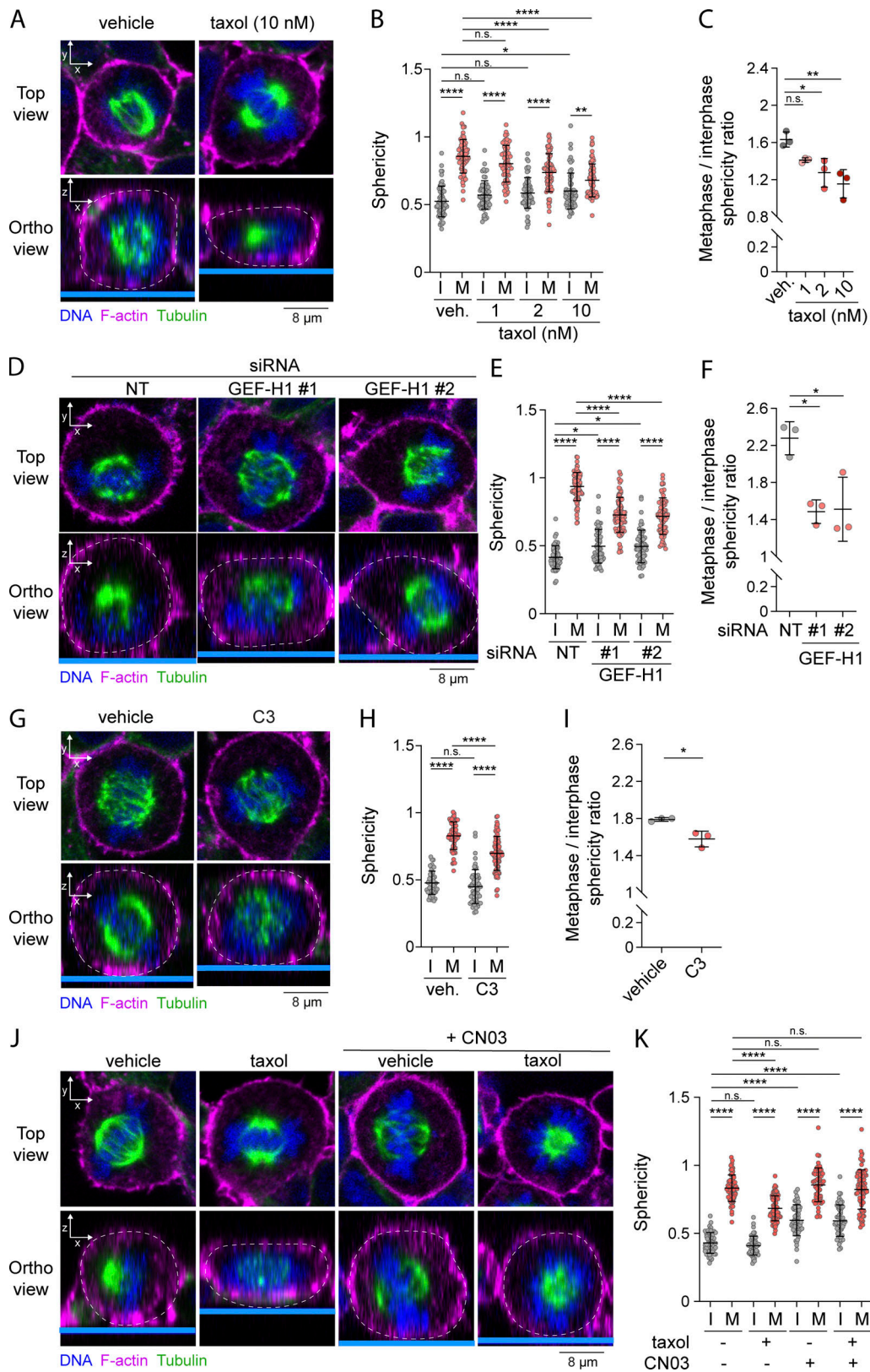
Figure 6. **Interphase microtubules disassembly at mitotic entry controls cell rounding in metaphase. (A–K)** Sphericity and mitotic rounding defects were measured using immunofluorescence 3D reconstitution after confocal microscopy in HEK293T cells incubated with vehicle (DMSO) or indicated concentrations of taxol for 90 min (A–C; $n > 60$ cells), transiently transfected with non-target siRNA (NT) or two independent siRNA targeting GEF-H1 (D–F; $n > 50$ cells), incubated with vehicle (veh.; water) or 1 μg/ml C3 transferase for 6 h (G–I; $n > 50$ cells), or incubated with vehicle (DMSO), 10 nM taxol for 90 min and/or 1 μg/ml Rho activator II (CN03) for 1 h (J and K; $n > 50$ cells). Sphericity was measured as in Fig. 3 G (B, E, H, and K). Mitotic rounding defects were assessed by measuring the mean sphericity ratio of metaphase to interphase cell populations (C, F, and I). **(A, D, G, and J)** Top panels show confocal planes (Top view), and

Leguay et al.
Signals that prompt metaphase cell rounding

Journal of Cell Biology   9 of 17
https://doi.org/10.1083/jcb.202109065

(Fig. 6, J and K; and Fig. S4, P and Q). These results, combined, establish that microtubule disassembly is a key regulator of metaphase cell rounding depending on RhoA activation.

Both GEF-H1 and Ect2 act upstream of RhoA to regulate ERM phosphorylation and cell rounding during mitosis

RhoA has been shown to be central to another signaling pathway that regulates reorganization of the actin cytoskeleton in early mitosis. RhoA is also activated by Ect2 (Miki et al., 1993; Yuce et al., 2005), a Rho-GEF that is itself phosphorylated and activated by Cdk1/Cyclin B (Hara et al., 2006; Matthews et al., 2012; Niiya et al., 2006). Ect2 promotes the generation of actomyosin forces dependently on ROCK kinases that phosphorylate myosin light chain II (Matthews et al., 2012). While SLK depletion and RhoA inhibition totally abrogated ERM activation in metaphase, GEF-H1 depletion or treatment with low dose of taxol only partially inhibited ERM activation (Fig. 4, A–H). We, therefore, hypothesized that interphase microtubule disassembly and Ect2 could act together to fully activate ERMs in metaphase. We found that depletion of Ect2 by independent siRNAs partially decreases ERM phosphorylation in metaphase, but did not affect ERM activation in interphase (Fig. 7, A and B; and Fig. S5 A). Therefore, similarly to GEF-H1, Ect2 contributes to ERM activation only in mitosis. Having confirmed that Ect2 is important for interphase-to-metaphase cell rounding (Matthews et al., 2012; Fig. 7, C and D; and Fig. S5, B–D), we then depleted Ect2 together with GEF-H1 and showed that this co-depletion further decreases ERM phosphorylation in metaphase when compared with single depletions of these Rho-GEFs (Fig. 7, E and F). We confirmed this result by depleting Ect2 and inhibiting the GEF-H1 signaling pathway using low dose of taxol to inhibit interphase microtubule disassembly (Fig. S5, E and F). In accordance with this discovery, we found that these two pathways act together to promote metaphase cell rounding. Ect2 and GEF-H1 depletion led to a similar decrease of cell sphericity in metaphase while their co-depletion further decreased this parameter (Fig. 7, G and H; and Fig. S5, G and H). The ratio of sphericity between the population of interphase and metaphase cells also tends to decrease upon double depletion of Ect2 and GEF-H1 when compared with single depletions, even if this reduction did not reach statistical significance (Fig. 7 I). We also confirmed that Ect2 and GEF-H1 act together to promote metaphase cell rounding by stabilizing microtubules with low dose of taxol in Ect2-depleted cells (Fig. S5, I and J). Altogether, our results provide evidence that Ect2 and GEF-H1 converge to RhoA to activate ERMs and cell rounding at mitotic entry.

Finally, since RhoA was shown to directly activate both SLK and ROCK kinases (Bagci et al., 2020), we aimed to investigate the respective roles of these kinases in rounding of metaphase cells. As previously reported (Maddox and Burridge, 2003), we found that ROCK inhibition using Y-27632 decreased cell rounding in metaphase (Fig. 7, J and K; and Fig. S5, K and L). We also found that SLK depletion promoted a higher attenuation in sphericity of metaphase cells when compared with ROCK inhibition that was not further potentiated when ROCK kinases were co-inhibited with SLK (Fig. 7, J and K). This indicates that coupling ROCK-dependent actin forces to the plasma membrane through SLK-ERM activation plays major roles in metaphase cell rounding.

Discussion

By performing a chemical screen using newly developed ERM biosensors (Leguay et al., 2021), we discovered that drugs that promote microtubule disassembly, such as nocodazole, activate ERMs through a GEF-H1–RhoA–SLK signaling axis. While nocodazole treatment was already known to promote rounding of cells in interphase, dependently on GEF-H1 and RhoA (Chang et al., 2008; Krendel et al., 2002), we now show that this also involves the ERM activating kinase SLK, since nocodazole no longer induces cell rounding when SLK is depleted. Interphase microtubules also disassemble at mitosis entry, and we obtained several experimental evidence demonstrating that this disassembly is one of the cell-cycle cues that control metaphase cell rounding through ERM activation. We found that (1) SLK or ERM depletion prevents normal cell rounding in metaphase; (2) expression of a constitutively active mutant of ezrin rescues normal levels of metaphase cell sphericity when SLK is depleted; (3) use of taxol to perturb interphase microtubule disassembly (Hornick et al., 2008; Leung and Cassimeris, 2019; McHedlishvili et al., 2018) prevents normal ERM activation and cell rounding in metaphase; (4) depletion of GEF-H1, a RhoA-GEF inhibited by its binding to microtubules (Joo and Olson, 2021) or inhibition of RhoA, prevents normal ERM activation and cell rounding in metaphase, similar to what is observed in taxol-treated cells; (5) both ERM phosphorylation and cell rounding defects in metaphase triggered by taxol treatment are rescued by bypassing the need of interphase microtubule disassembly through chemical activation of RhoA.

Interestingly as cells are entering into mitosis, microtubules are progressively disassembled at the cell periphery, whereas they are stabilized at the vicinity of the cortex by taxol (Leung and Cassimeris, 2019). It is therefore tempting to speculate that at mitosis entry, GEF-H1 is released and activated by local microtubule disassembly close to the cortex where ERMs need to be activated to contribute to metaphase cell rounding. We are currently testing this hypothesis, which is also in agreement with a recent study showing that in migrating cells, microtubules that disassemble close to the cortex promote cortical contractions depending on GEF-H1 and RhoA activation within a narrow cortical peripheral band (Azoitei et al., 2019).

We propose that disassembly of interphase microtubules at mitotic entry activates the membrane-actin linkers ERMs

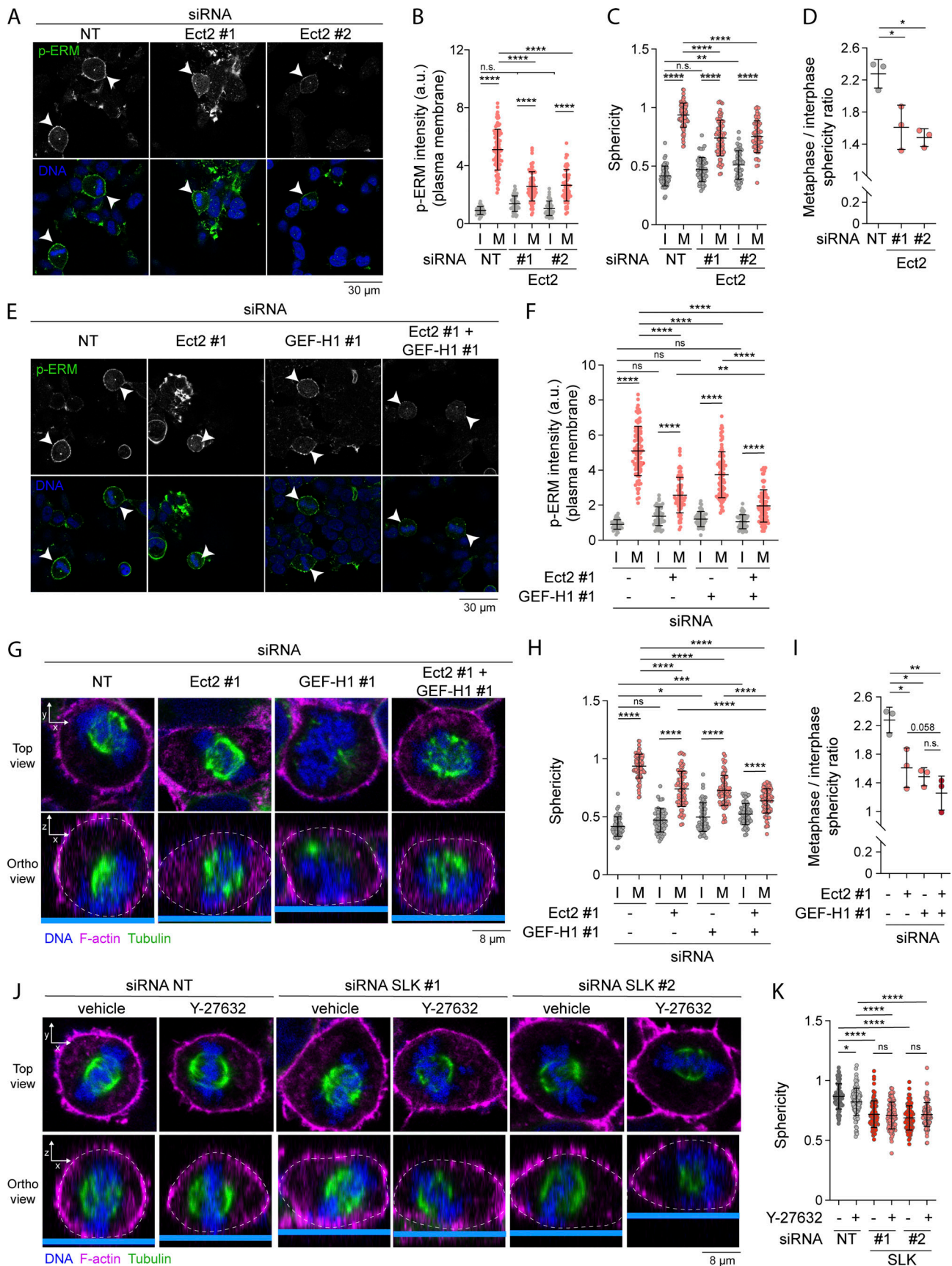Figure 7. **Both GEF-H1 and Ect2 regulate ERM phosphorylation and cell rounding in metaphase. (A and B)** Immunofluorescence of HEK293T cells transiently transfected with non-target siRNA (NT) or two independent siRNA targeting Ect2 (A). Metaphase and interphase cells were identified based on DNA

Leguay et al.
Signals that prompt metaphase cell rounding

Journal of Cell Biology 11 of 17
https://doi.org/10.1083/jcb.202109065

staining (DAPI, blue; A; arrowheads indicate metaphase cells), and p-ERM (green) signal intensity at the plasma membrane was quantified and normalized to interphase cells transfected with non-target siRNA (B; n > 60 cells). **(C and D)** Sphericity and mitotic rounding defects were measured using immunofluorescence 3D reconstitution after confocal microscopy (see Fig. S5 B) in HEK293T cells transiently transfected with non-target siRNA (NT) or two independent siRNA targeting Ect2. Sphericity was measured as in Fig. 3 G (C). Mitotic rounding defects were assessed by measuring the mean sphericity ratio of metaphase to interphase cell populations (D). (n > 55 cells). **(E and F)** Immunofluorescence of HEK293T cells transiently transfected with non-target siRNA (NT), siRNA targeting GEF-H1 and/or siRNA targeting Ect2 (E). Metaphase and interphase cells were identified based on DNA staining (DAPI, blue; E; arrowheads indicate metaphase cells), and p-ERM signal intensity at the plasma membrane was quantified and normalized to interphase cells transfected with non-target siRNA (F). Quantifications of p-ERM signal intensity of cells transfected with non-target siRNA or siRNA #1 targeting Ect2 (Ect2 #1; F) were already shown in B (n > 45 cells). **(G–K)** Sphericity and mitotic rounding defects were measured using immunofluorescence 3D reconstitution after confocal microscopy in HEK293T cells transiently transfected with non-target siRNA (NT), siRNA targeting GEF-H1 and/or siRNA targeting Ect2 (G–I; n > 55 cells), or two independent siRNA targeting SLK and incubated with vehicle (DMSO) or 10 µM Y-27632 for 4 h (J and K; n > 55 cells). Sphericity was measured as in Fig. 3 G (H and K). Mitotic rounding defects were assessed by measuring the mean sphericity ratio of metaphase to interphase cell populations (I). Quantifications of sphericity of cells transiently transfected with non-target siRNA or siRNA #1 targeting Ect2 (Ect2 #1; H) were already shown in C. Quantifications of sphericity of metaphase cells transiently transfected with non-target siRNA or siRNA targeting SLK and treated with vehicle (K) were already shown in Fig. 5 B. **(G and J)** Top panels show confocal planes (Top view), and lower panels show orthogonal views (Ortho view). I, interphase; M, metaphase. Immunofluorescences (A, E, G, and J) are representative of three independent experiments. Quantifications of p-ERM, sphericity, and sphericity ratio of metaphase-to-interphase populations represent the mean ± SD of three independent experiments. Dots represent individual cells (B, C, F, H, and K) or independent experiments (D and I). P values were calculated using Holm-Sidak's multiple comparisons test with a single pooled variance (B, C, F, H, and K) or using a two-tailed paired t test (D and I). *, P < 0.05; **, P < 0.01; ***, P < 0.001; ****, P < 0.0001.

through GEF-H1, RhoA, and SLK (Fig. 8). Interphase microtubule disassembly was shown to depend on the inactivation of MAP7, a microtubule-stabilizing protein, through direct phosphorylation by the Cdk1/Cyclin B complex (McHedlishvili et al., 2018). Therefore, at mitosis onset, Cdk1/Cyclin B activates two Rho-GEFs: GEF-H1 through disassembly of interphase microtubule (McHedlishvili et al., 2018) and Ect2 through direct phosphorylation (Matthews et al., 2012). GEF-H1 and Ect2 both engage RhoA that relays the cell-cycle signals to its direct effectors, ROCK kinases, and SLK. In return, ROCK kinases generate the actomyosin forces (Maddox and Burridge, 2003; Matthews et al., 2012), while SLK activates ERMs that link these forces to the plasma membrane (Fig. 8). This integrated signaling network coordinates the generation of actomyosin forces with their coupling to the plasma membrane to drive cell rounding at mitotic entry.

Slik and dMoesin, the respective *Drosophila* orthologs of SLK and ERMs, have been shown to be essential to promote metaphase cell rounding by increasing cortical stiffness (Kunda et al., 2008). Yet, the importance of SLK and ERMs for mitotic cell rounding remained controversial. In HeLa cells, ezrin RNAi-mediated silencing was previously shown to trigger a decrease in cortical tension during metaphase (Toyoda et al., 2017). Since the increase of cortical tension at mitotic entry provides an essential force that prompts cell rounding, this finding suggests that the role of ERMs for metaphase rounding is conserved in mammalian cells. In disagreement with this hypothesis, metaphase rounding was reported not to be affected upon depletion of SLK or ERMs in HeLa cells (Machicoane et al., 2014). Notably, these last observations were made by recording cell division by phase contrast time-lapse microscopy. Although this approach could indicate whether cells round-up to a certain extent, it is not as accurate as 3D reconstruction after confocal microscopy to precisely measure cell sphericity. Here, using the latter approach, we demonstrated that depletion of SLK or co-depletion of the three ERMs promote a decrease of cell sphericity between interphase and metaphase when compared to control cells. This establishes that Slik/SLK and ERM proteins play important roles for metaphase cell rounding from fly to mammals.

We showed that the inhibition of Ect2, GEF-H1, RhoA, ROCK kinases, SLK, or ERMs triggered substantial defects in metaphase cell rounding. Yet, we did not observe a complete inhibition of this rounding. We also found that while the overexpression of a constitutive active mutant of ezrin (ezrin^{T567D}) did increase cell rounding in interphase, the average sphericity of interphase ezrin^{T567D} expressing cells was still lower than what was observed in control metaphase cells or in ezrin^{T567D} metaphase cells (Fig. 5 J). These results suggest that the reorganization of actomyosin network at mitotic entry is an important but not a sufficient mechanism to drive cell rounding in metaphase.

This is in agreement with other studies that showed that mitotic cell rounding is also promoted by two other mechanisms: the decrease of integrin-based cell-substrate adhesions (Dao et al., 2009; Marchesi et al., 2014; Yamakita et al., 1999) and the increase of intracellular pressure due to water influx (Son et al., 2015; Stewart et al., 2011; Zlotek-Zlotkiewicz et al., 2015). In addition to help cell rounding, the water influx occurring in metaphase was shown to help the disassembly of interphase microtubules (McHedlishvili et al., 2018). Yet, it is still not clear whether and how the reorganization of the actomyosin cortex at mitotic entry is coordinated with focal adhesion disassembly. A potential candidate that could coordinate these two mechanisms is SLK. This kinase was shown to directly phosphorylate paxillin and to promote focal adhesion turnover during cell migration (Quizi et al., 2013; Wagner et al., 2008). We are currently investigating whether, in addition to activating ERMs, SLK could promote the disassembly of focal adhesion structures when cells enter mitosis.

To remodel cell shape, the forces generated by actomyosin contractions need to be linked to the plasma membrane. While the ROCK kinases are well-characterized RhoA effectors, we very recently reported that SLK is also a direct effector of this small GTPase (Bagci et al., 2020). This finding provided a potential signaling module that places RhoA in an upstream setting to couple actomyosin force generation, via ROCK, with their functional integration through ERM activation, via SLK, at the plasma membrane. Here, we demonstrated that this signaling module was at play to drive mitotic rounding. It is indeed
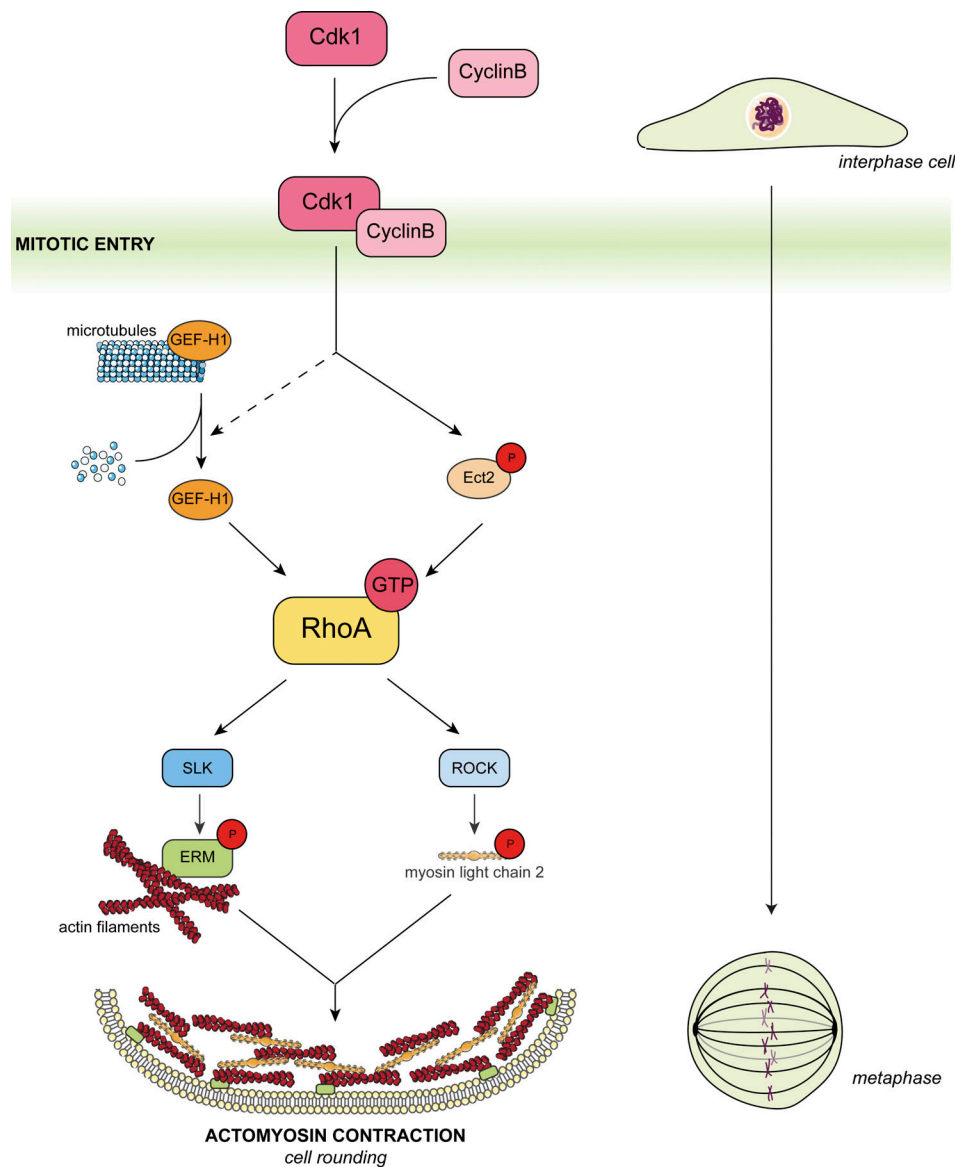
Figure 8. **Model for ERM activation and cell rounding at mitosis entry.** The Cdk1/Cyclin B complex promotes both Ect2 phosphorylation (Matthews et al., 2012) and interphase microtubule disassembly (McHedlishvili et al., 2018), leading to GEF-H1 release and activation. GEF-H1 and Ect2 activate RhoA that in turn activates SLK and ROCK kinases. While ROCK kinases take charge of the phosphorylation of myosin II to generate actomyosin forces, SLK activates ERMs that integrate the actomyosin forces to the plasma membrane. This integrated signaling network promotes cell rounding at mitotic entry.

tempting to speculate that this signaling module can regulate other aspects of cell morphogenesis. Interestingly, GEF-H1 was recently shown to be specifically inhibited at the proximity of focal adhesions. GEF-H1, under its inactive state, is bound to microtubules that are themselves linked to talin by a KN motif and ankyrin repeat domain-containing protein/CLIP-associating protein microtubule docking complex (Rafiq et al., 2019). This mechanism ensures that actomyosin contractions are minimal at the vicinity of focal adhesions. This raises the possibility that the disassembly of focal adhesions releases active GEF-H1 to activate RhoA and promote actomyosin contractions coupled to the plasma membrane through activation of ROCK and ERMs. While this remains to be tested, one could envision that this signaling pathway can drive the dynamic reorganization of the plasma

membrane necessary for migration, a cellular function that was also shown to involve activity of ERMs (Arpin et al., 2011; Clucas and Valderrama, 2014).

Materials and methods

Reagents and inhibitors
Nocodazole, taxol, and Y-27632 were purchased from Sigma-Aldrich (#M1404, #T7402, and #688000, respectively). Podo-phyllotoxin was purchased from Cayman chemical (#19575). The exoenzyme C3 transferase (Rho inhibitor I) and the Rho acti-vator II (CN03) were purchased from Cytoskeleton (#CT04 and #CN03, respectively). Coelenterazine 400a was purchased from NanoLight Technology (#340).

DNA and RNA constructs

MyrPB-ezrin-rLucII, ezrin-rLucII, and rGFP-CAAX constructs were previously described (Leguay et al., 2021). Ezrin^{KK211,212MM}-rLucII was obtained by inverse PCR from ezrin-rLucII using the following primers: (forward) 5′-ATGATGGGAACAGACCTTTGGCTTGGAGTTGATGCCCTTGG-3′; (reverse) 5′-GTTTTTTATCTCGAAATAGTTGATTCCATACATTTCCAGGTCC-3′.

Ezrin-DsRed was obtained by subcloning PCR amplified ezrin into pDsRed-Monomer-N1 vector (#632465; Clontech) digested by NheI and XhoI. Ezrin^{T567D}-DsRed and ezrin^{T567A}-DsRed were obtained by inverse PCR on ezrin-DsRed using the following primers: (forward for TD) 5′-AAGATCTGCGGCAGATCCGGCAGGGCAACACCAAGC-3′; (forward for TA) 5′-AAGCTTTGCGGCAGATCCGGCAGGGCAACACCAAGC-3′; (reverse for TD/TA) 5′-TGTACTTGTCCCGGCCTTGCCTCATGTTCTCG-3′.

MISSION shRNA constructs were obtained in pLKO.1-puro vectors from Sigma-Aldrich: SLK #1 (TRCN0000000895, sense strand: 5′-CCACCACTGATGAACCTGAAA-3′); SLK #2 (TRCN0000000897, sense strand: 5′-CCATGACAGAACAGCAGTAAT-3′); GEF-H1 #1 (TRCN0000003174, sense strand: 5′-CGCTCTGTCCATCGAAACTTT-3′); GEF-H1 #2 (TRCN0000003176, sense strand: 5′-CCCAACCTGCAATGTGACTAT-3′).

FlexiTube siRNA were obtained from Qiagen: SLK #1 (SI00107723, sense strand: 5′-TAGCATCTTGTGATCACCCAA-3′); SLK #2 (SI04438350, sense strand: 5′-AAGTAGCATCTTGGTGACTAA-3′); GEF-H1 #1 (SI00067564, sense strand: 5′-CTGCAATGTGACTATCCACAA-3′); GEF-H1 #2 (SI05181533, sense strand: 5′-TTCAGTGGTATCGCTGCAGAA-3′); ECT2 #1 (SI02643067, sense strand: 5′-TTGCCTAGAGATAGCAAGAAA-3′); ECT2 #2 (SI03049249, sense strand: 5′-ATGACGCATATTAATGAGGAT-3′); EZR (SI02664228, sense strand: 5′-CAGGACTGATTGAATTACGGA-3′); RDX (SI02664144, sense strand: 5′-GAGGAAGAACGTGTAACCGAA-3′); MSN (SI00300888, sense strand: 5′-AAAGGTTTCTCCACCTGGCTG-3′).

Cell culture, transfection and infection

Human HEK293T, HeLa, A375, SW620 cells, and murine MC38 cells were cultured in DMEM (4.5 g/l D-glucose, L-Glutamine, 110 mg/l sodium pyruvate; #11995073; Invitrogen) supplemented with 10% FBS (#12483020; Life Invitrogen) and 1% penicillin–streptomycin antibiotics (#15070063; Thermo Fisher Scientific) at 37°C with 5% CO$_2$. Transfections for BRET experiments were performed as previously described (Leguay et al., 2021). Briefly, HEK293T cells were transfected with 1 μg of total DNA (50 ng rLucII construct, 300 ng rGFP-CAAX, and 650 ng salmon sperm DNA) using linear polyethyleneimine (#43896; Alfa Aesar) as transfecting agent (polyethyleneimine:DNA ratio of 3:1). Transfected cells were then plated in white 96-well culture plates (#82050-736; VWR) and incubated for 48 h prior to BRET measurement. For loss-of-function experiments, siRNAs were transfected using lipofectamine RNAiMAX (#13778075; Thermo Fisher Scientific). For lentiviral infection, lentiviruses were added to the cells cultivated in DMEM supplemented with 10% FBS and 5 μg/ml polybrene (#H9268; Sigma-Aldrich) for 48 h. Infected cells were then selected for another 48 h prior to experiments using 2 μg/ml puromycin (#540222; EMD Millipore).

BRET measurement

48 h after transfection, HEK293T cells were washed with HBSS (#14065056; Thermo Fisher Scientific) and incubated for 5 min with 2.5 μM coelenterazine 400a diluted in HBSS. BRET signals were monitored with a Tecan Infinite 200 PRO multifunctional microplate reader (Tecan) equipped with BLUE1 (370–480 nm; donor) and GREEN1 (520–570 nm; acceptor) filters. BRET signals were calculated as a ratio by dividing the acceptor emission over the donor emission.

Chemical screen

The day before the experiment, HEK293T cells stably expressing MyrPB-ezrin-rLucII and rGFP-CAAX were suspended in DMEM/F12 without phenol red (#21041025; Invitrogen) supplemented with 1% FBS, sifted through a 70-μm cell strainer (#352350; Falcon), and seeded in white 384-well culture plates (#3570; Corning). After an overnight incubation at 37°C with 5% CO$_2$, compounds from different libraries (Microsource Discovery, Biomol GmbH, Prestwick, and Sigma-Aldrich) were added using an Echo 555 acoustic dispenser (Labcyte) at a final concentration of 10 μM for 1 h. Substrate solution (coelenterazine 400a diluted in HBSS with 1% pluronic acid) was added 15 min before reading at a final concentration of 2.5 μM. BRET signals were monitored with a Synergy NEO HTS microplate reader (BioTek) equipped with a donor filter of 410/80 nm and an acceptor filter of 515/40 nm.

Immunoblotting

Cells were washed with ice-cold PBS and lysed in TLB buffer (40 mM Hepes, 1 mM EDTA, 120 mM NaCl, 10 mM NaPPi, 10% glycerol, 1% Triton X-100, 0.1% SDS) supplemented with both phosphatase and protease inhibitors (phosphatase inhibitor cocktail [#P2850; Sigma-Aldrich], 1 mM sodium orthovanadate [Na$_3$VO$_4$, #S6508; Sigma-Aldrich], 5 mM β-glycerophosphate [#G6251; Sigma-Aldrich], 1 mM PMSF [#P7626; Sigma-Aldrich], and anti-protease cocktail [#4693132001; Sigma-Aldrich]). Samples were then boiled in sample buffer (200 mM Tris-HCl 1 M, pH 6.8, 8% SDS, 0.4% bromophenol blue, 40% glycerol, and 412 mM β-mercaptoethanol) before being resolved by 8% SDS-PAGE and transferred to nitrocellulose membranes (pore 0.2 μm, #27376-991; VWR). For RhoA immunoblotting, proteins were transferred to polyvinylidene difluoride membrane (pore 0.45 μm, #IPVH00010; Millipore). Membranes were then blocked in TBS-Tween (25 mM Tris-HCl, pH 8, 125 mM NaCl, 0.1% Tween 20) supplemented with 2% BSA (#ALB001.250; Bioshop) for 1 h before overnight incubation with primary antibodies at 4°C. Primary antibodies used are: rabbit anti-ERM (1:1,000, #3142; Cell Signaling), rabbit anti-ezrin (1:1,000, #3145; Cell Signaling), rabbit anti-radixin (1:1,000, #2636; Cell Signaling), rabbit anti-moesin (1:1,000, #3150; Cell Signaling), rabbit anti-phospho-ERM (1:5,000; Carreno et al., 2008), mouse anti-actin (1:5,000, #MAB1501; Sigma-Aldrich), rabbit anti-SLK (1:500, #A300-499A; Cederlane), mouse anti-RhoA (1:500, #ARH05; Cytoskeleton), rabbit anti–GEF-H1 (1:1,000, #ab155785; Abcam), rabbit anti-Ect2 (1:1,000, #07–1364; Millipore Sigma), and mouse anti-tubulin (1:1,000, #T9026; Sigma-Aldrich). Washed membranes were

then incubated for 1 h with secondary antibodies: goat anti-rabbit HRP antibody (1:10,000, #sc-2004; Santacruz) or goat anti-mouse HRP (1:10,000, #sc-516102; Santacruz). Protein detection was performed using Amersham ECL Western blotting detection reagent (#CA95038-564L; GE Healthcare). Immunoblots were quantified using ImageJ software (National Institutes of Health [NIH]).

Immunofluorescence
Cells plated on glass coverslips (#0115200; Marienfeld) were washed once with PBS and fixed. For p-ERM and p-MLC2 staining, cells were fixed with 10% trichloroacetic acid (#T0699; Sigma-Aldrich) for 10 min at room temperature before extensive washings with TBS (20 mM Tris-HCl, pH 7.5, 154 mM NaCl, 2 mM EGTA, 2 mM MgCl$_2$). For cytoskeleton staining, cells were fixed with 4% paraformaldehyde (#043368-9M; Cederlane) for 30 min. Cells were then permeabilized with 0.02% saponin (#0163; Amresco) and blocked with 2% BSA (#ALB001.250; Bioshop) for 1 h. The antibodies used were the following: rabbit anti-phospho-ERM (1:500, overnight; Carreno et al., 2008), mouse anti-phospho-MLC2 (Ser19; 1:50, overnight, #3675S; Cell signaling), goat anti-rabbit Alexa Fluor 488–conjugated secondary antibody (1:200, 1 h, #A11070; Invitrogen), goat anti-mouse Alexa Fluor 488–conjugated secondary antibody (1:200, 1 h, #A21235; Invitrogen), phalloidin Texas red (1:100, 1 h, #T7471; Life technologies), phalloidin Alexa Fluor 647 (1:100, 1 h, #A22287; Thermo Fisher Scientific) and anti–α-Tubulin-FITC (1:200, 1 h, #F2168; Millipore Sigma). Coverslips were mounted in Vectashield medium with DAPI (#H-1200; Vector Laboratories). Images were acquired using a LSM700 confocal microscope (Zeiss) equipped with a Plan Neofluar 40×/1.30 NA or a Plan Apochromat DIC 63×/1.4 oil immersion objectives. For quantifications of p-ERM levels, images were acquired with identical microscope settings across the same experiment. p-ERM signals were measured all around the plasma membrane using the segmented line tool from ImageJ software (NIH). p-ERM intensity is represented as the average of p-ERM levels at the plasma membrane per cell, in which background was subtracted. In experiments where p-ERM levels were quantified in both interphase and metaphase cells, p-ERM levels per cell were normalized to the average of p-ERM levels in interphase control cells (vehicle or si/shRNA non-target). Thus, the average of normalized p-ERM levels in control interphase cells is equal to 1. For cell sphericity measurements, orthogonal views were extracted using Zen software (Zeiss). On these views, several parameters were measured using ImageJ software (NIH): cell height (z) and cell width determined as the average between the longer axis (L) and its orthogonal (O). Cell sphericity was then determined as a ratio between cell height and cell width. Blue lines on pictures symbolize the adhesion surface (coverslip).

In vitro kinase assay
In vitro kinase assays were performed as previously described with slight modifications (Bagci et al., 2020). Briefly, endogenous SLK from HEK293T cell lysate was immunoprecipitated using rabbit anti-SLK antibody (#A300-499A; Bethyl) incubated for 1 h at 4°C followed by incubation with protein A–sepharose

beads (#GE17-0780-01; GE Healthcare) for 2 h at 4°C. Beads were then washed three times with TLB and three times with kinase reaction buffer (50 mM Tris-HCl, pH 7.5, 100 mM NaCl, 6 mM MgCl$_2$, and 1 mM MnCl$_2$). Beads were then resuspended in 15 μl kinase reaction buffer supplemented with 2 mM DTT, 50 μM ATP, 1 mM Na$_3$VO$_4$, 5 mM NaF, and 2.5 mM sodium pyrophosphate with purified recombinant GST or GST-Ezrin$^{479–585}$ from BL21 bacteria. Beads were finally incubated at 30°C for 30 min, and proteins were denatured using sample buffer. For in vitro kinase assay using recombinant purified SLK, SLK enzyme was purchased from Promega (#V4242). In vitro kinase assays were performed in 384-well low volume plates (#784075; Greiner) in 5 μl reaction volume. Kinase reactions were executed for 2 h at room temperature in reaction buffer A (40 mM Tris, pH 7.5, 20 mM MgCl$_2$ and 0.1 mg/ml BSA supplemented with 50 μM DTT) with 100 ng purified SLK, 0.5 μg histone H3 protein as substrate, and 50 μM ATP. Kinase reactions were then stopped and processed using ADP-Glo kinase assay kit (#V6930; Promega) as indicated in the manual. Briefly, 5 μl of ADP-Glo reagent was added for 40 min at room temperature to stop the reaction, followed by 10 μl of Kinase Detection Agent for 30 min. Luminescence signals was measured with a Synergy NEO Microplate Reader (Biotek).

Rhotekin-RBD pull-down assay
Rhotekin-RBD beads were purchased from Cytoskeleton (#RT02), and the assay were performed as indicated by the manufacturer. Briefly, HEK293T cells, treated as indicated, were washed once with ice-cold PBS and lysed in ice-cold cell lysis buffer (50 mM Tris, pH 7.5, 10 mM MgCl$_2$, 0.5 M NaCl, and 2% IGEPAL) supplemented with protease inhibitor cocktail. Cell lysates were then immediately clarified by centrifugation at 10,000 g for 1 min at 4°C. After protein quantification, 600 μg of proteins were incubated with 50 μg rhotekin-RBD beads for 1 h at 4°C. Beads were then washed twice with washing buffer (25 mM Tris, pH 7.5, 30 mM MgCl$_2$, 40 mM NaCl) and suspended in sample buffer.

Data and statistical analysis
All quantifications were performed using ImageJ software (NIH) and analyzed using GraphPad PRISM software (GraphPad Software). Microscopy images were prepared using ImageJ software (NIH) and Photoshop (Adobe). All data represent the mean ± SD of multiple independent experiments as indicated in the figure legends. Statistical significance between various conditions was assessed by determining P values (95% confidence interval) using GraphPad PRISM software. Different statistical tests were used according to the type of data, as indicated in the figure legends: one-sample t test (one experimental group compared to a control experimental group normalized to 1); two-tailed paired or unpaired t test (two experimental groups); Holm-Sidak's multiple comparison test with a single pooled variance (three or more experimental groups). Data distribution was assumed to be normal, but this was not formally tested.

Online supplemental material
Fig. S1 presents the list of molecules identified in the chemical screen and shows that drugs that disassemble microtubules

trigger ERM phosphorylation. Fig. S2 validates the efficiency of small molecules targeting ROCK and RhoA used in this study. It shows the impact of taxol on mitotic spindle formation and confirms the role of GEF-H1 on ERM activation. Fig. S3 presents measurements of cell height and cell shape within the x/y plane from experiments presented in Fig. 5 showing that SLK and ERMs promote cell rounding in metaphase. Fig. S4 presents measurements of cell height and cell shape within the x/y plane from experiments presented in Fig. 6 showing that both GEF-H1 and RhoA are promoting cell rounding in metaphase. Fig. S5 presents measurements from experiments presented in Fig. 7 showing that both Ect2 and GEF-H1 regulate ERM phosphorylation and cell rounding in metaphase.

Acknowledgments

References

Arpin, M., D. Chirivino, A. Naba, and I. Zwaenepoel. 2011. Emerging role for ERM proteins in cell adhesion and migration. *Cell Adh. Migr.* 5:199–206. https://doi.org/10.4161/cam.5.2.15081

Azoitei, M.L., J. Noh, D.J. Marston, P. Roudot, C.B. Marshall, T.A. Daugird, S.L. Lisanza, M.-J. Sandí, M. Ikura, J. Sondek, et al. 2019. Spatiotemporal dynamics of GEF-H1 activation controlled by microtubule- and Src-mediated pathways. *J. Cell Biol.* 218:3077–3097. https://doi.org/10.1083/jcb.201812073

Bagci, H., N. Sriskandarajah, A. Robert, J. Boulais, I.E. Elkholi, V. Tran, Z.Y. Lin, M.P. Thibault, N. Dube, D. Faubert, et al. 2020. Mapping the proximity interaction network of the Rho-family GTPases reveals signalling pathways and regulatory mechanisms. *Nat. Cell Biol.* 22:120–134. https://doi.org/10.1038/s41556-019-0438-7

Ben-David, U., and A. Amon. 2020. Context is everything: Aneuploidy in cancer. *Nat. Rev. Genet.* 21:44–62. https://doi.org/10.1038/s41576-019-0171-x

Birkenfeld, J., P. Nalbant, B.P. Bohl, O. Pertz, K.M. Hahn, and G.M. Bokoch. 2007. GEF-H1 modulates localized RhoA activation during cytokinesis under the control of mitotic kinases. *Dev. Cell*. 12:699–712. https://doi.org/10.1016/j.devcel.2007.03.014

Birukova, A.A., D. Adyshev, B. Gorshkov, G.M. Bokoch, K.G. Birukov, and A.D. Verin. 2006. GEF-H1 is involved in agonist-induced human pulmonary endothelial barrier dysfunction. *Am. J. Physiol. Lung Cell. Mol. Physiol.* 290:L540–L548. https://doi.org/10.1152/ajplung.00259.2005

Breton, B., E. Sauvageau, J. Zhou, H. Bonin, C. Le Gouill, and M. Bouvier. 2010. Multiplexing of multicolor bioluminescence resonance energy transfer. *Biophys. J.* 99:4037–4046. https://doi.org/10.1016/j.bpj.2010.10.025

Carreno, S., I. Kouranti, E.S. Glusman, M.T. Fuller, A. Echard, and F. Payre. 2008. Moesin and its activating kinase Slik are required for cortical stability and microtubule organization in mitotic cells. *J. Cell Biol.* 180:739–746. https://doi.org/10.1083/jcb.200709161

Chang, Y.C., H.H. Lee, Y.J. Chen, G.M. Bokoch, and Z.F. Chang. 2006. Contribution of guanine exchange factor H1 in phorbol ester-induced apoptosis. *Cell Death Differ.* 13:2023–2032. https://doi.org/10.1038/sj.cdd.4401901

Chang, Y.C., P. Nalbant, J. Birkenfeld, Z.F. Chang, and G.M. Bokoch. 2008. GEF-H1 couples nocodazole-induced microtubule disassembly to cell contractility via RhoA. *Mol. Biol. Cell*. 19:2147–2153. https://doi.org/10.1091/mbc.e07-12-1269

Clucas, J., and F. Valderrama. 2014. ERM proteins in cancer progression. *J. Cell Sci.* 127:267–275. https://doi.org/10.1242/jcs.133108

Dao, V.T., A.G. Dupuy, O. Gavet, E. Caron, and J. de Gunzburg. 2009. Dynamic changes in Rap1 activity are required for cell retraction and spreading during mitosis. *J. Cell Sci.* 122:2996–3004. https://doi.org/10.1242/jcs.041301

De Jamblinne, C.V., B. Decelle, M. Dehghani, M. Joseph, N. Sriskandarajah, K. Leguay, B. Rambaud, S. Lemieux, P.P. Roux, D.R. Hipfner, and S. Carreno. 2020. STRIPAK regulates Slik localization to control mitotic morphogenesis and epithelial integrity. *J. Cell Biol.* 219:e201911035. https://doi.org/10.1083/jcb.201911035

Diz-Munoz, A., D.A. Fletcher, and O.D. Weiner. 2013. Use the force: Membrane tension as an organizer of cell shape and motility. *Trends Cell Biol.* 23:47–53. https://doi.org/10.1016/j.tcb.2012.09.006

Fehon, R.G., A.I. McClatchey, and A. Bretscher. 2010. Organizing the cell cortex: The role of ERM proteins. *Nat. Rev. Mol. Cell Biol.* 11:276–287. https://doi.org/10.1038/nrm2866

Fujisawa, K., P. Madaule, T. Ishizaki, G. Watanabe, H. Bito, Y. Saito, A. Hall, and S. Narumiya. 1998. Different regions of Rho determine Rho-selective binding of different classes of Rho target molecules. *J. Biol. Chem.* 273:18943–18949. https://doi.org/10.1074/jbc.273.30.18943

Gary, R., and A. Bretscher. 1995. Ezrin self-association involves binding of an N-terminal domain to a normally masked C-terminal domain that includes the F-actin binding site. *Mol. Biol. Cell.* 6:1061–1075. https://doi.org/10.1091/mbc.6.8.1061

Gautreau, A., D. Louvard, and M. Arpin. 2000. Morphogenic effects of ezrin require a phosphorylation-induced transition from oligomers to monomers at the plasma membrane. *J. Cell Biol.* 150:193–203. https://doi.org/10.1083/jcb.150.1.193

Hara, T., M. Abe, H. Inoue, L.R. Yu, T.D. Veenstra, Y.H. Kang, K.S. Lee, and T. Miki. 2006. Cytokinesis regulator ECT2 changes its conformation through phosphorylation at Thr-341 in G2/M phase. *Oncogene*. 25:566–578. https://doi.org/10.1038/sj.onc.1209078

Hornick, J.E., J.R. Bader, E.K. Tribble, K. Trimble, J.S. Breunig, E.S. Halpin, K.T. Vaughan, and E.H. Hinchcliffe. 2008. Live-cell analysis of mitotic spindle formation in taxol-treated cells. *Cell Motil. Cytoskeleton*. 65:595–613. https://doi.org/10.1002/cm.20283

Joo, E., and M.F. Olson. 2021. Regulation and functions of the RhoA regulatory guanine nucleotide exchange factor GEF-H1. *Small GTPases*. 12(5–6):358–371. https://doi.org/10.1080/21541248.2020.1840889

Kotani, H., K. Takaishi, T. Sasaki, and Y. Takai. 1997. Rho regulates association of both the ERM family and vinculin with the plasma membrane in MDCK cells. *Oncogene*. 14:1705–1713. https://doi.org/10.1038/sj.onc.1200998

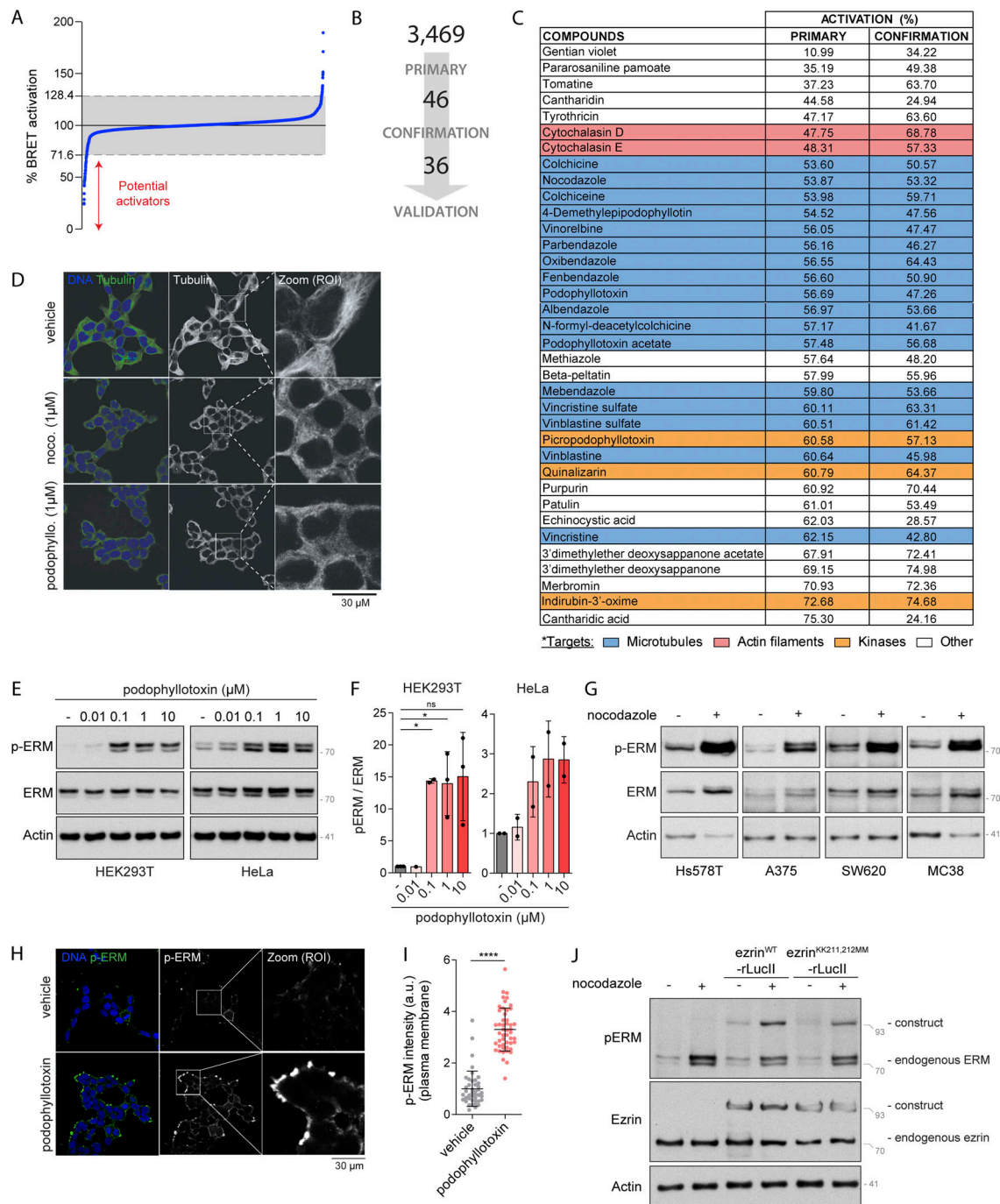Krendel, M., F.T. Zenke, and G.M. Bokoch. 2002. Nucleotide exchange factor GEF-H1 mediates cross-talk between microtubules and the actin cytoskeleton. *Nat. Cell Biol.* 4:294–301. https://doi.org/10.1038/ncb773

Kunda, P., A.E. Pelling, T. Liu, and B. Baum. 2008. Moesin controls cortical rigidity, cell rounding, and spindle morphogenesis during mitosis. *Curr. Biol.* 18:91–101. https://doi.org/10.1016/j.cub.2007.12.051
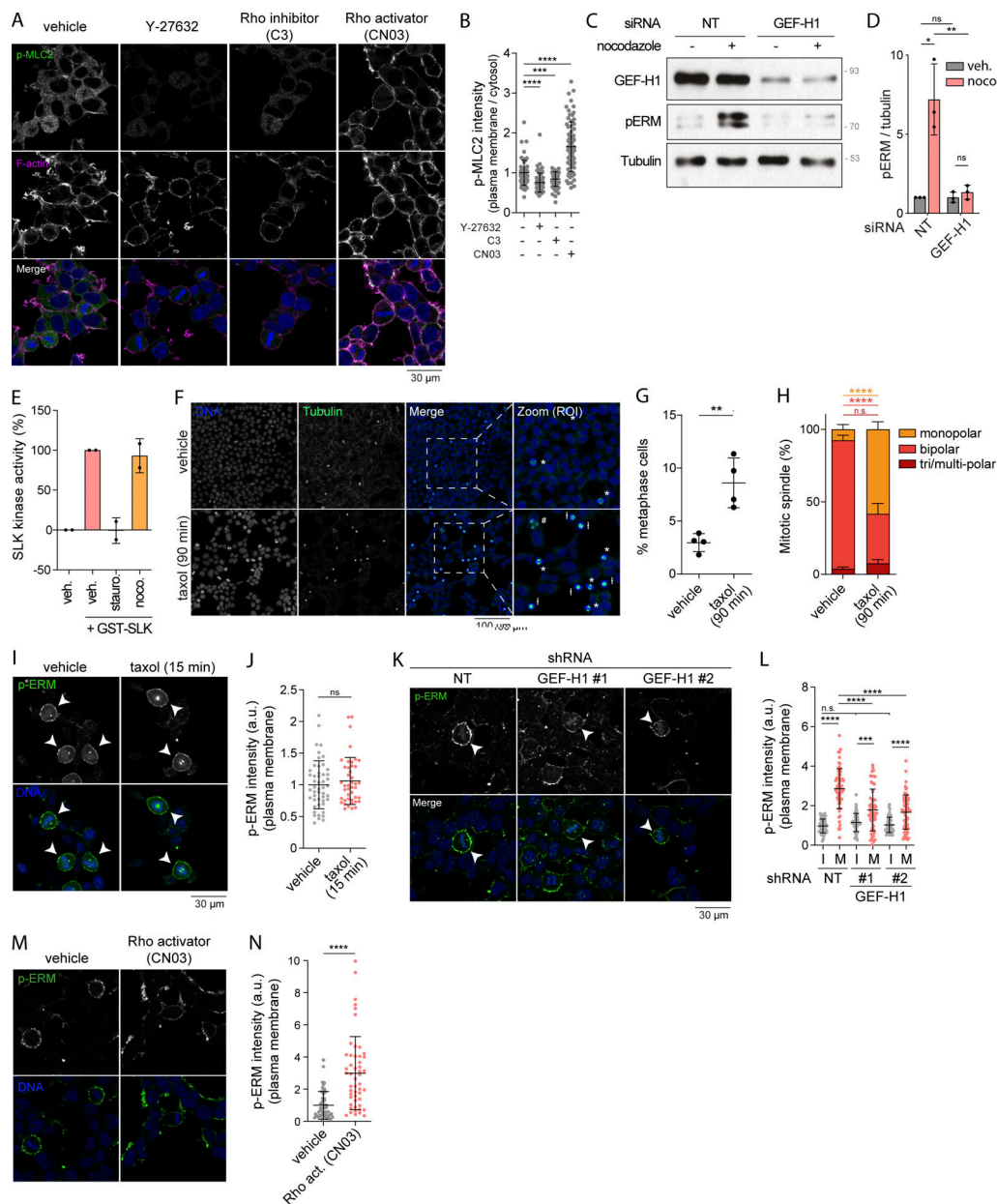
Lancaster, O.M., M. Le Berre, A. Dimitracopoulos, D. Bonazzi, E. Zlotek-Zlot-kiewicz, R. Picone, T. Duke, M. Piel, and B. Baum. 2013. Mitotic rounding alters cell geometry to ensure efficient bipolar spindle formation. *Dev. Cell.* 25:270–283. https://doi.org/10.1016/j.devcel.2013.03.014

Leguay, K., B. Decelle, Y.Y. He, A. Pagniez, M. Hogue, H. Kobayashi, C. Le Gouill, M. Bouvier, and S. Carreno. 2021. Development of conformational BRET biosensors that monitor ezrin, radixin and moesin activation in real time. *J. Cell Sci.* 134:jcs255307. https://doi.org/10.1242/jcs.255307

Leung, J.C., and L. Cassimeris. 2019. Reorganization of paclitaxel-stabilized microtubule arrays at mitotic entry: Roles of depolymerizing kinesins and severing proteins. *Cancer Biol. Ther.* 20:1337–1347. https://doi.org/10.1080/15384047.2019.1638678

Machicoane, M., C.A. de Frutos, J. Fink, M. Rocancourt, Y. Lombardi, S. Garel, M. Piel, and A. Echard. 2014. SLK-dependent activation of ERMs controls LGN-NuMA localization and spindle orientation. *J. Cell Biol.* 205:791–799. https://doi.org/10.1083/jcb.201401049

Maddox, A.S., and K. Burridge. 2003. RhoA is required for cortical retraction and rigidity during mitotic cell rounding. *J. Cell Biol.* 160:255–265. https://doi.org/10.1083/jcb.200207130

Majumdar, M., T.M. Seasholtz, D. Goldstein, P. de Lanerolle, and J.H. Brown. 1998. Requirement for Rho-mediated myosin light chain phosphorylation in thrombin-stimulated cell rounding and its dissociation from mitogenesis. *J. Biol. Chem.* 273:10099–10106. https://doi.org/10.1074/jbc.273.17.10099

Marchesi, S., F. Montani, G. Deflorian, R. D'Antuono, A. Cuomo, S. Bologna, C. Mazzoccoli, T. Bonaldi, P.P. Di Fiore, and F. Nicassio. 2014. DEPDC1B coordinates de-adhesion events and cell-cycle progression at mitosis. *Dev. Cell.* 31:420–433. https://doi.org/10.1016/j.devcel.2014.09.009

Matsui, T., S. Yonemura, S. Tsukita, and S. Tsukita. 1999. Activation of ERM proteins in vivo by Rho involves phosphatidyl-inositol 4-phosphate 5-kinase and not ROCK kinases. *Curr. Biol.* 9:1259–1262. https://doi.org/10.1016/s0960-9822(99)80508-9

Matsuzawa, T., A. Kuwae, S. Yoshida, C. Sasakawa, and A. Abe. 2004. Enteropathogenic Escherichia coli activates the RhoA signaling pathway via the stimulation of GEF-H1. *EMBO J.* 23:3570–3582. https://doi.org/10.1038/sj.emboj.7600359

Matthews, H.K., U. Delabre, J.L. Rohn, J. Guck, P. Kunda, and B. Baum. 2012. Changes in Ect2 localization couple actomyosin-dependent cell shape changes to mitotic progression. *Dev. Cell.* 23:371–383. https://doi.org/10.1016/j.devcel.2012.06.003

Matthews, H.K., S. Ganguli, K. Plak, A.V. Taubenberger, Z. Win, M. Williamson, M. Piel, J. Guck, and B. Baum. 2020. Oncogenic signaling alters cell shape and mechanics to facilitate cell division under confinement. *Dev. Cell.* 52:563–573.e3. https://doi.org/10.1016/j.devcel.2020.01.004

McHedlishvili, N., H.K. Matthews, A. Corrigan, and B. Baum. 2018. Two-step interphase microtubule disassembly aids spindle morphogenesis. *BMC Biol.* 16:14. https://doi.org/10.1186/s12915-017-0478-z

Miki, T., C.L. Smith, J.E. Long, A. Eva, and T.P. Fleming. 1993. Oncogene ect2 is related to regulators of small GTP-binding proteins. *Nature.* 362:462–465. https://doi.org/10.1038/362462a0

Niiya, F., T. Tatsumoto, K.S. Lee, and T. Miki. 2006. Phosphorylation of the cytokinesis regulator ECT2 at G2/M phase stimulates association of the mitotic kinase Plk1 and accumulation of GTP-bound RhoA. *Oncogene.* 25:827–837. https://doi.org/10.1038/sj.onc.1209124

Pelaseyed, T., R. Viswanatha, C. Sauvanet, J.J. Filter, M.L. Goldberg, and A. Bretscher. 2017. Ezrin activation by LOK phosphorylation involves a PIP2-dependent wedge mechanism. *Elife.* 6:e22759. https://doi.org/10.7554/eLife.22759

Quizi, J.L., K. Baron, K.N. Al-Zahrani, P. O'Reilly, R.K. Sriram, J. Conway, A.A. Laurin, and L.A. Sabourin. 2013. SLK-mediated phosphorylation of paxillin is required for focal adhesion turnover and cell migration. *Oncogene.* 32:4656–4663. https://doi.org/10.1038/onc.2012.488

Rafiq, N.B.M., Y. Nishimura, S.V. Plotnikov, V. Thiagarajan, Z. Zhang, S. Shi, M. Natarajan, V. Viasnoff, P. Kanchanawong, G.E. Jones, and A.D. Bershadsky. 2019. A mechano-signalling network linking microtubules, myosin IIA filaments and integrin-based adhesions. *Nat. Mater.* 18:638–649. https://doi.org/10.1038/s41563-019-0371-y

Ramanathan, S.P., J. Helenius, M.P. Stewart, C.J. Cattin, A.A. Hyman, and D.J. Muller. 2015. Cdk1-dependent mitotic enrichment of cortical myosin II promotes cell rounding against confinement. *Nat. Cell Biol.* 17:148–159. https://doi.org/10.1038/ncb3098

Ramkumar, N., and B. Baum. 2016. Coupling changes in cell shape to chromosome segregation. *Nat. Rev. Mol. Cell Biol.* 17:511–521. https://doi.org/10.1038/nrm.2016.75

Ren, Y., R. Li, Y. Zheng, and H. Busch. 1998. Cloning and characterization of GEF-H1, a microtubule-associated guanine nucleotide exchange factor for Rac and Rho GTPases. *J. Biol. Chem.* 273:34954–34960. https://doi.org/10.1074/jbc.273.52.34954

Roubinet, C., B. Decelle, G. Chicanne, J.F. Dorn, B. Payrastre, F. Payre, and S. Carreno. 2011. Molecular networks linked by Moesin drive remodeling of the cell cortex during mitosis. *J. Cell Biol.* 195:99–112. https://doi.org/10.1083/jcb.201106048

Sahai, E., T. Ishizaki, S. Narumiya, and R. Treisman. 1999. Transformation mediated by RhoA requires activity of ROCK kinases. *Curr. Biol.* 9:136–145. https://doi.org/10.1016/s0960-9822(99)80067-0

Schmidt, G., P. Sehr, M. Wilm, J. Selzer, M. Mann, and K. Aktories. 1997. Gln 63 of Rho is deamidated by Escherichia coli cytotoxic necrotizing factor-1. *Nature.* 387:725–729. https://doi.org/10.1038/42735

Shaw, R.J., M. Henry, F. Solomon, and T. Jacks. 1998. RhoA-dependent phosphorylation and relocalization of ERM proteins into apical membrane/actin protrusions in fibroblasts. *Mol. Biol. Cell.* 9:403–419. https://doi.org/10.1091/mbc.9.2.403

Solinet, S., K. Mahmud, S.F. Stewman, K. Ben El Kadhi, B. Decelle, L. Talje, A. Ma, B.H. Kwok, and S. Carreno. 2013. The actin-binding ERM protein Moesin binds to and stabilizes microtubules at the cell cortex. *J. Cell Biol.* 202:251–260. https://doi.org/10.1083/jcb.201304052

Son, S., J.H. Kang, S. Oh, M.W. Kirschner, T.J. Mitchison, and S. Manalis. 2015. Resonant microchannel volume and mass measurements show that suspended cells swell during mitosis. *J. Cell Biol.* 211:757–763. https://doi.org/10.1083/jcb.201505058

Stewart, M.P., J. Helenius, Y. Toyoda, S.P. Ramanathan, D.J. Muller, and A.A. Hyman. 2011. Hydrostatic pressure and the actomyosin cortex drive mitotic cell rounding. *Nature.* 469:226–230. https://doi.org/10.1038/nature09642

Taubenberger, A.V., B. Baum, and H.K. Matthews. 2020. The mechanics of mitotic cell rounding. *Front. Cell Dev. Biol.* 8:687. https://doi.org/10.3389/fcell.2020.00687

Totsukawa, G., Y. Yamakita, S. Yamashiro, D.J. Hartshorne, Y. Sasaki, and F. Matsumura. 2000. Distinct roles of ROCK (Rho-kinase) and MLCK in spatial regulation of MLC phosphorylation for assembly of stress fibers and focal adhesions in 3T3 fibroblasts. *J. Cell Biol.* 150:797–806. https://doi.org/10.1083/jcb.150.4.797

Toyoda, Y., C.J. Cattin, M.P. Stewart, I. Poser, M. Theis, T.V. Kurzchalia, F. Buchholz, A.A. Hyman, and D.J. Muller. 2017. Genome-scale single-cell mechanical phenotyping reveals disease-related genes involved in mitotic rounding. *Nat. Commun.* 8:1266. https://doi.org/10.1038/s41467-017-01147-6

Viswanatha, R., P.Y. Ohouo, M.B. Smolka, and A. Bretscher. 2012. Local phosphocycling mediated by LOK/SLK restricts ezrin function to the apical aspect of epithelial cells. *J. Cell Biol.* 199:969–984. https://doi.org/10.1083/jcb.201207047

Wagner, S., C.J. Storbeck, K. Roovers, Z.Y. Chaar, P. Kolodziej, M. McKay, and L.A. Sabourin. 2008. FAK/src-family dependent activation of the Ste20-like kinase SLK is required for microtubule-dependent focal adhesion turnover and cell migration. *PLoS One.* 3:e1868. https://doi.org/10.1371/journal.pone.0001868

Yamakita, Y., G. Totsukawa, S. Yamashiro, D. Fry, X. Zhang, S.K. Hanks, and F. Matsumura. 1999. Dissociation of FAK/p130(CAS)/c-Src complex during mitosis: Role of mitosis-specific serine phosphorylation of FAK. *J. Cell Biol.* 144:315–324. https://doi.org/10.1083/jcb.144.2.315

Yuce, O., A. Piekny, and M. Glotzer. 2005. An ECT2-centralspindlin complex regulates the localization and function of RhoA. *J. Cell Biol.* 170:571–582. https://doi.org/10.1083/jcb.200501097

Zhai, Y., P.J. Kronebusch, P.M. Simon, and G.G. Borisy. 1996. Microtubule dynamics at the G2/M transition: Abrupt breakdown of cytoplasmic microtubules at nuclear envelope breakdown and implications for spindle morphogenesis. *J. Cell Biol.* 135:201–214. https://doi.org/10.1083/jcb.135.1.201

Zlotek-Zlotkiewicz, E., S. Monnier, G. Cappello, M. Le Berre, and M. Piel. 2015. Optical volume and mass measurements show that mammalian cells swell during mitosis. *J. Cell Biol.* 211:765–774. https://doi.org/10.1083/jcb.201505056

Supplemental material

COMPOUNDS	ACTIVATION (%)	
	PRIMARY	CONFIRMATION
Gentian violet	10.99	34.22
Pararosaniline pamoate	35.19	49.38
Tomatine	37.23	63.70
Cantharidin	44.58	24.94
Tyrothricin	47.17	63.60
Cytochalasin D	47.75	68.78
Cytochalasin E	48.31	57.33
Colchicine	53.60	50.57
Nocodazole	53.87	53.32
Colchiceine	53.98	59.71
4-Demethylepipodophyllotin	54.52	47.56
Vinorelbine	56.05	47.47
Parbendazole	56.16	46.27
Oxibendazole	56.55	64.43
Fenbendazole	56.60	50.90
Podophyllotoxin	56.69	47.26
Albendazole	56.97	53.66
N-formyl-deacetylcolchicine	57.17	41.67
Podophyllotoxin acetate	57.48	56.68
Methiazole	57.64	48.20
Beta-peltatin	57.99	55.96
Mebendazole	59.80	53.66
Vincristine sulfate	60.11	63.31
Vinblastine sulfate	60.51	61.42
Picropodophyllotoxin	60.58	57.13
Vinblastine	60.64	45.98
Quinalizarin	60.79	64.37
Purpurin	60.92	70.44
Patulin	61.01	53.49
Echinocystic acid	62.03	28.57
Vincristine	62.15	42.80
3'dimethylether deoxysappanone acetate	67.91	72.41
3'dimethylether deoxysappanone	69.15	74.98
Merbromin	70.93	72.36
Indirubin-3'-oxime	72.68	74.68
Cantharidic acid	75.30	24.16

*Targets: ▢ Microtubules ▢ Actin filaments ▢ Kinases ▢ Other

Figure S1. **Microtubule disassembly promotes ERM activation. (A)** Distribution of the 3,469 compounds (blue dots) screened over MyrPB-ezrin-rLucII BRET2 activation. BRET2 signals are normalized to vehicle (DMSO, 100%). Grey zone represents vehicle (100%) ± 28.4% corresponding to three times the SD of all compounds tested. Compounds promoting a BRET2 signal decrease lower than 71.6% are potential ezrin activators. **(B)** Schematic representation of the number of hits identified after both the primary and confirmation screens. **(C)** Table showing the targets of each compounds identified and validated in the chemical screen. BRET2 signals (in % compared to vehicle) measured for each compound in the primary and confirmation screens are indicated in columns 2 and 3, respectively. **(D)** Immunofluorescence of microtubules of HEK293T cells treated with indicated inhibitors for 15 min. **(E and F)** Immunoblots of HEK293T (left) and HeLa (right) cells incubated with the indicated concentrations of podophyllotoxin for 15 min (E). p-ERM over ERM signals were quantified and normalized to vehicle (DMSO; F). **(G)** Immunoblots of Hs578T, A375, SW620, and MC38 cells treated with 1 µM nocodazole for 15 min. **(H and I)** Immunofluorescence of HEK293T cells incubated with vehicle (DMSO) or 1 µM podophyllotoxin for 15 min (H). p-ERM staining at the plasma membrane was quantified and normalized to cells treated with vehicle (I; $n > 45$ cells). Immunofluorescence (H) and quantification of p-ERM staining at the plasma membrane (I) of vehicle treated cells were already shown in Fig. 1, H and I, respectively. **(J)** Immunoblot of HEK293T cells transfected with ezrin[WT]-rLucII or ezrin[KK211,212MM]-rLucII and treated with vehicle (DMSO) or 1 µM nocodazole for 15 min. Immunofluorescences (D and H) and immunoblots (E, G, and J) are representative of at least two independent experiments. p-ERM quantifications represent the mean ± SD of at least two independent experiments. Dots represent independent experiments (F) or individual cells (I). P values were calculated using one-sample t test (F) or using two-tailed unpaired t test (I). *, P < 0.05; ****, P < 0.0001. Numbers associated with Western blots indicate molecular weight in kD. Source data are available for this figure: SourceData FS1.

Leguay et al.
Signals that prompt metaphase cell rounding

Journal of Cell Biology   S2
https://doi.org/10.1083/jcb.202109065

Figure S2. **Taxol-induced microtubule stabilization affects mitotic spindle organization while GEF-H1 and RhoA are key regulators of ERM during mitosis. (A and B)** Immunofluorescence of HEK293T cells treated with vehicle (DMSO), 10 µM Y-27632 for 4 h, 1 µg/ml C3 transferase (C3) for 6 h, or 1 µg/ml Rho activator II (CN03) for 1 h (A). p-MLC2 (Ser19) signal intensity at the plasma membrane over cytosol is normalized to cells treated with vehicle (B; n > 60 cells). **(C and D)** Immunoblot of HEK293T cells transiently transfected with non-target siRNA (NT) or siRNA targeting GEF-H1 (C). p-ERM over tubulin signals were quantified and normalized to NT treated with vehicle (D). **(E)** SLK kinase activity measured by an in vitro kinase assay in presence of purified GST-SLK pre-incubated with vehicle (DMSO), 100 nM staurosporine, or 1 µM nocodazole for 15 min. **(F–H)** Immunofluorescence of HEK293T cells treated with vehicle (DMSO) or 10 nM taxol for 90 min (F). Percentage of metaphase cells was determined (G) based on DNA and tubulin staining (F), and mitotic spindles were classified following the number of apparent centrosomes (monopolar, bipolar, or tri/multi-polar; H). **(I and J)** Immunofluorescence of HEK293T cells treated with vehicle (DMSO) or 10 nM taxol for 15 min (I). Metaphase cells were identified based on DNA staining (DAPI, blue; arrowheads indicate metaphase cells), and p-ERM signal intensity at the plasma membrane was quantified and normalized to cells treated with vehicle (J; n > 50 cells). **(K and L)** Immunofluorescence of HEK293T cells stably expressing non-target shRNA (NT) or two independent shRNA targeting GEF-H1 (K). Metaphase and interphase cells were identified based on DNA staining (DAPI, blue; arrowheads indicate metaphase cells), and p-ERM signal intensity at the plasma membrane was quantified and normalized to interphase cells treated with non-target shRNA (L). I, interphase; M, metaphase (n > 55 cells). **(M and N)** Immunofluorescence of HEK293T cells incubated with vehicle (water) or 1 µg/ml Rho activator II (CN03) for 1 h (M). p-ERM signal intensity at the plasma membrane in metaphase cells was quantified and normalized to cells incubated with vehicle (N; n = 50 cells). Immunofluorescences (A, F, I, K, and M) and immunoblot (C) are representative of at least two independent experiments. All quantifications represent the mean ± SD of at least two independent experiments. Dots represent individual cells (B, J, L, and N) or independent experiments (D, E, and G). P values were calculated using a two-tailed unpaired t test (B, J, and N), using a two-tailed paired t test (G and H), or using Holm-Sidak's multiple comparisons test with a single pooled variance (D and L), except for comparison made with normalizing condition (NT + vehicle [D]) where one-sample t test was applied. *, P < 0.05; **, P < 0.01; ***, P < 0.001; ****, P < 0.0001. Numbers associated with Western blots indicate molecular weight in kD. Source data are available for this figure: SourceData FS2.
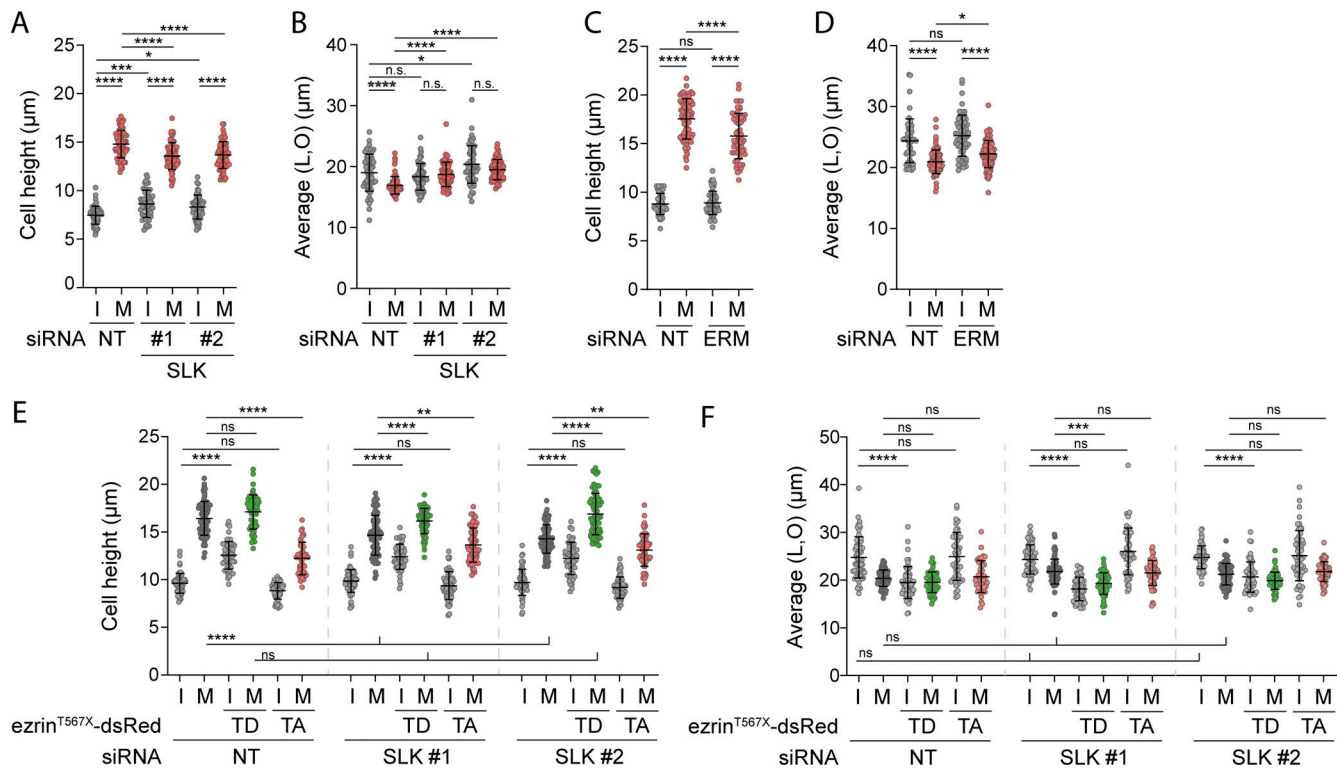
Figure S3. **SLK and ERMs control metaphase cell rounding. (A–F)** Cell height and cell shape within the x/y plane were measured in HEK293T cells transiently transfected with non-target siRNA (NT) or two independent siRNA targeting SLK (A and B; $n > 55$ cells), or a combination of three independent siRNA targeting all three ERM (C and D; $n > 55$ cells), or two independent siRNA targeting SLK and co-transfected with ezrin^{T567D}-dsRed (constitutively active) or ezrin^{T567A}-dsRed (non phosphorylatable) constructs (E and F; $n > 48$ cells). I, interphase; M, metaphase. Quantifications represent the mean ± SD of three independent experiments. Dots represent individual cells. P values were calculated using Holm-Sidak's multiple comparisons test with a single pooled variance. *, $P < 0.05$; **, $P < 0.01$; ***, $P < 0.001$; ****, $P < 0.0001$.
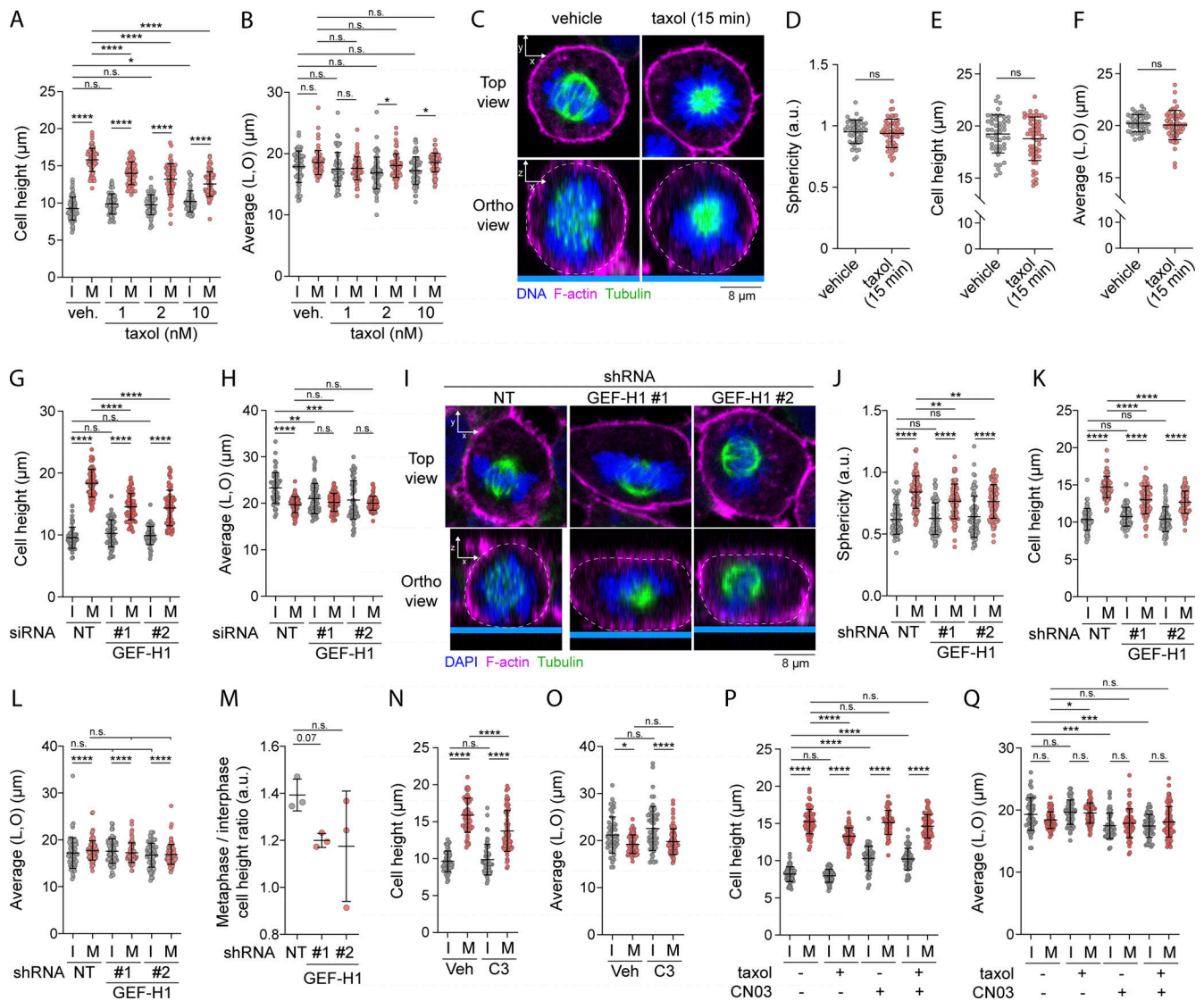
Figure S4. **Microtubule dissociation at mitotic entry regulates cell rounding depending on GEF-H1 and RhoA. (A and B)** Cell height and cell shape within the x/y plane were measured in HEK293T cells incubated with vehicle (DMSO) or taxol for 90 min (A and B; $n > 60$ cells). **(C–F)** Sphericity (D), cell height (E), and cell shape within the x/y plane (F) were measured using immunofluorescence 3D reconstitution after confocal microscopy (C) in HEK293T metaphase cells treated with vehicle (DMSO) or 10 nM taxol for 15 min. Sphericity was measured as in Fig. 3 G (D). **(C)** Top panels show confocal planes (Top view), and lower panels show orthogonal views (Ortho view; $n > 45$ cells). **(G and H)** Cell height (G) and cell shape within the x/y plane (H) were measured in HEK293T cells transiently transfected with non-target siRNA (NT) or two independent siRNA targeting GEF-H1 ($n > 50$ cells). **(I–M)** Sphericity (J), cell height (K), cell shape within the x/y plane (L), and mitotic rounding defects (M) were measured using immunofluorescence 3D reconstitution after confocal microscopy (I) in HEK293T cells stably expressing non-target shRNA (NT) or two independent shRNA targeting GEF-H1. Sphericity was measured as in Fig. 3 G (F). Mitotic rounding defects were assessed by measuring the mean sphericity ratio of metaphase-to-interphase cell populations (M). **(I)** Top panels show confocal planes (Top view), and lower panels show orthogonal views (Ortho view; $n > 70$ cells). **(N–Q)** Cell height and cell shape within the x/y plane were measured in HEK293T cells incubated with vehicle (water) or 1 μg/ml C3 transferase for 6 h (N and O; $n > 50$ cells), or incubated with vehicle (DMSO), 10 nM taxol for 90 min and/or 1 μg/ml Rho activator II (CN03) for 1 h (P and Q; $n > 50$ cells). I, interphase; M, metaphase. Immunofluorescences (C and I) are representative of at least two independent experiments. All quantifications represent the mean ± SD of at least two independent experiments. Dots represent individual cells (A, B, D–H, J–L, and N–Q) or independent experiments (M). P values were calculated using Holm-Sidak's multiple comparisons test with a single pooled variance (A, B, G, H, J–L, and N–Q), two-tailed unpaired t test (D–F) or two-tailed paired t test (M). *, $P < 0.05$; **, $P < 0.01$; ***, $P < 0.001$; ****, $P < 0.0001$.

Leguay et al.
Signals that prompt metaphase cell rounding

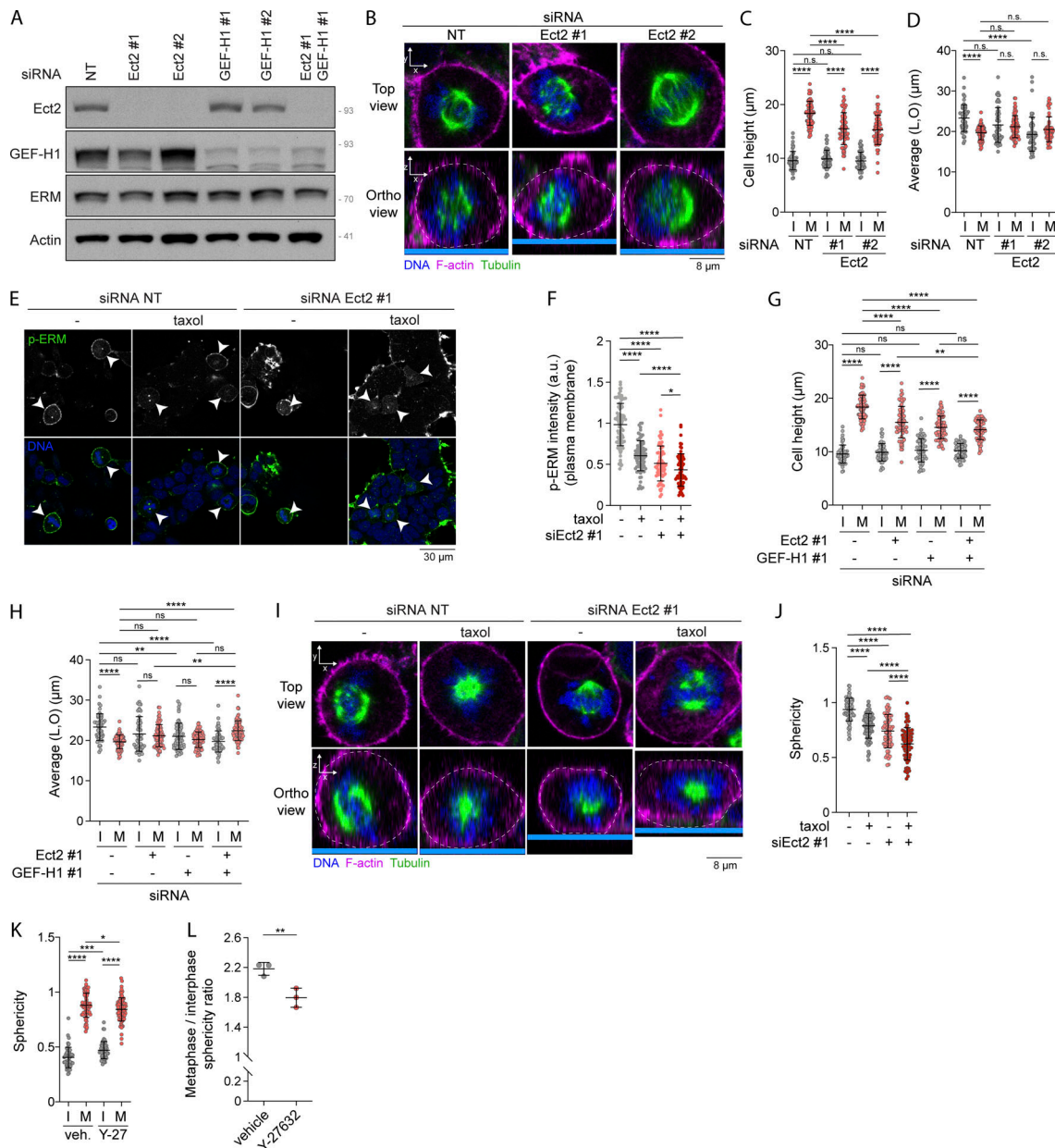Journal of Cell Biology   S5
https://doi.org/10.1083/jcb.202109065

Figure S5. Ect2 acts together with interphase microtubule disassemblyand GEF-H1 to regulate ERM activity and metaphase cell rounding.
(A) Immunoblot of HEK293T cells transiently transfected with non-target siRNA (NT; lane #1), two independent siRNA targeting Ect2 (lanes #2 and #3), or GEF-H1 (lanes #4 and #5), or transfected with a combination of siRNA targeting Ect2 and GEF-H1 (lane #6). **(B–D)** Cell height (C) and cell shape within the x/y plane (D) were measured using immunofluorescence 3D reconstitution after confocal microscopy (B) in HEK293T cells transiently transfected with non-target siRNA (NT) or two independent siRNA targeting Ect2 (*n* > 55 cells). **(E and F)** Immunofluorescence of HEK293T cells transiently transfected with non-target siRNA (NT) or siRNA targeting Ect2 and incubated with vehicle (DMSO) or 10 nM taxol for 90 min. Metaphase cells were identified based on DNA staining (DAPI, blue; E; arrowheads indicate metaphase cells), and p-ERM signal intensity at the plasma membrane in metaphase cells was quantified and normalized to cells transfected with non-target siRNA and incubated with vehicle (F). Quantification of p-ERM signal intensity of metaphase cells transiently transfected with non-target siRNA (NT) or siRNA #1 targeting Ect2 (Ect2 #1) was already shown in Fig. 7 B (*n* > 70 cells). **(G and H)** Cell height (G) and cell shape within the x/y plane (H) were measured in HEK293T cells transiently transfected with non-target siRNA (NT), siRNA targeting Ect2 or GEF-H1, or with a combination of siRNA targeting Ect2 and GEF-H1 (*n* > 55 cells). **(I and J)** Sphericity was measured using immunofluorescence 3D reconstitution after confocal microscopy (I) in HEK293T cells transfected with non-target siRNA (NT) or siRNA targeting Ect2 and incubated with vehicle (DMSO) or 10 nM taxol for 90 min. Sphericity was measured as in Fig. 3 G (J). Sphericity of metaphase cells transiently transfected with non-target siRNA (NT) or siRNA #1 targeting Ect2 (Ect2 #1; J) was already shown in Fig. 7 C (*n* > 60 cells). **(K and L)** Sphericity (K) and mitotic rounding defects (L) were measured using immunofluorescence 3D reconstitution after confocal microscopy (see Fig. 7 J) in HEK293T cells incubated with vehicle (DMSO) or 10 µM Y-27632 for 4 h. Sphericity was measured as in Fig. 3 G (K). Mitotic rounding defects were assessed by measuring the mean sphericity ratio of metaphase to interphase cell populations (L) (*n* > 55 cells). I, interphase; M, metaphase. Immunoblot (A) and immunofluorescences (B, E, and I) are representative of three independent experiments. All quantifications represent the mean ± SD of three independent experiments. Dots represent individual cells (C, D, F–H, J, and K) or independent experiments (L). P values were calculated using Holm-Sidak's multiple comparisons test with a single pooled variance (C, D, F–H, J, and K) or two-tailed paired *t* test (L). *, P < 0.05; **, P < 0.01; ***, P < 0.001; ****, P < 0.0001. Numbers associated with Western blots indicate molecular weight in kD. Source data are available for this figure: SourceData FS5.